ELSEVIER

ARTICLE INFO

Keywords:

ABSTRACT

Published by Elsevier B.V.

1. Introduction

Fluvial sediments can contain exceptional records of climate change at timescales ranging from less than a year (e.g., drought or flood events) to multimillennial (e.g., glacial-interglacial cycles). Because alluvial rivers are relatively common on most of Earth's land masses, fluvial sediments are among the most accessible terrestrial records of responses to natural and human-influenced external forcings. Alluvial deposition and erosion are highly influenced by changes in climate, which exerts controls on water and sediment availability, and base level, which affects the amount of energy available to a fluvial system for transporting its water and sediment loads. This study focuses on fluvial system responses to large-scale changes in sea level and climate over the most recent glacial-interglacial cycle. An island setting was chosen because all of its major drainages flow directly into the ocean, so we can be reasonably confident that a direct coupling exists between sea-level changes and river system responses, eliminating (or at least minimizing) the influences of indirect forcings or local base levels.

The concept of base level, first introduced by John Wesley Powell (1875) and later refined by Davis (1902); Mackin (1948); Schumm (1993), and others, has been critically important to understanding the physical and sedimentological responses of fluvial systems to climate change. A simple definition of base level is the lowest elevation to which a river can erode its bed, the ultimate base level being sea level (Powell, 1875). Of course, sea level itself is not static, having fluctuated many times over the course of Earth's history. During the Quaternary, for example, sea level changed by more than 100 m, driven by mass transfer between oceans and glaciers during glacial-interglacial cycles (Murray-Wallace and Woodroffe, 2014). Other causes of relative sea-level changes include tectonically or isostatically driven uplift or subsidence of the land surface. When base level changes, a river may adjust

* Corresponding author.

its length, width, depth, channel roughness, sinuosity, gradient, and/or pattern in order to achieve the amount of energy needed to move its water and sediment loads downstream (Mackin, 1948; Schumm, 1993). If channel pattern and/or hydraulic geometry changes are not possible, or are insufficient to adjust for the base-level change, the river will aggrade or incise its bed.

In general, rivers tend to incise when base level is lowered and to aggrade in response to a rising base level. However, rivers typically respond to perturbations in a complex manner, in some cases even appearing to respond in ways that are opposite of expected, making simple cause-effect relationships difficult to determine. The reason for this is that rivers are controlled by allogenic (external) and autogenic (internal) forcings that may be interacting on concurrent or different temporal and spatial scales. For example, a wave of incision initiated by falling sea level may rejuvenate tributaries, causing deposition in the main channel. The temporarily stored sediment raises the local base level of the tributaries, and as the tributaries readjust, their sediment load decreases, so the main channel is once again able to transport the accumulated sediment downstream. As sediment is flushed from the main channel, the tributaries are again rejuvenated, and the cycle repeats (Schumm, 1973; Slingerland and Snow, 1988), resulting in a pulsed sediment delivery that is expressed in multiple downstream depositional events in response to the single external forcing. One product of this may be alluvial beds that are more localized in their spatial extent and thus are not necessarily traceable or correlative for long distances up- or downstream.

In more general terms, our ability to recognize and correctly interpret the evidence of climate change in the fluvial sedimentary record is confounded by the complexity of river response to external forcings. Elements of this complexity include (i) spatial and temporal scale, in that deposition could be occurring in one reach of a river while another reach is experiencing erosion; (ii) convergence, in which different causes can produce similar effects; (iii) divergence, in which similar causes or processes can produce different responses; (iv) variable sensitivity of systems to external forcings because of differing thresholds for change (Schumm and Brakenridge, 1987); and (v) complex response to external forcings due to internal system dynamics (Schumm, 1973; Blum and Tornqvist, 2000). Because of these, fluvial system responses to climate change may appear to have quite localized extents, or responses may seem inconsistent between neighboring or nearby drainages. Determining a regionally coherent sequence of events, therefore, requires a systematic approach to geologic investigations in a representative number of rivers or drainage areas.

Santa Rosa Island, in Channel Islands National Park, California, USA, is ideal for this study because it is relatively small in area, which allows examination of its fluvial systems in their entirety from headwaters to mouths. It has multiple drainages, which enables collection of a rich data set and facilitates distinguishing local from islandwide processes, forcings, and effects. The island has an essentially uniform climate, and all of its major drainages terminate at the ocean. Thus, we can assume that major external forcings, i.e., climate conditions (primarily precipitation amount, intensity, and seasonality) and sea-level changes acted uniformly and simultaneously (at least in a geologic sense) on all of the drainage systems on the island.

2. Physical setting

Santa Rosa Island (SRI) is the second largest of the California Channel Islands (Fig. 1), measuring ~25 km long and 16 km wide, with an area of 215 km^2, and elevations ranging from sea level to 480 m. It is part of the group of four east-west aligned islands that make up the northern Channel Islands chain, located roughly 50 km southwest of Santa Barbara and

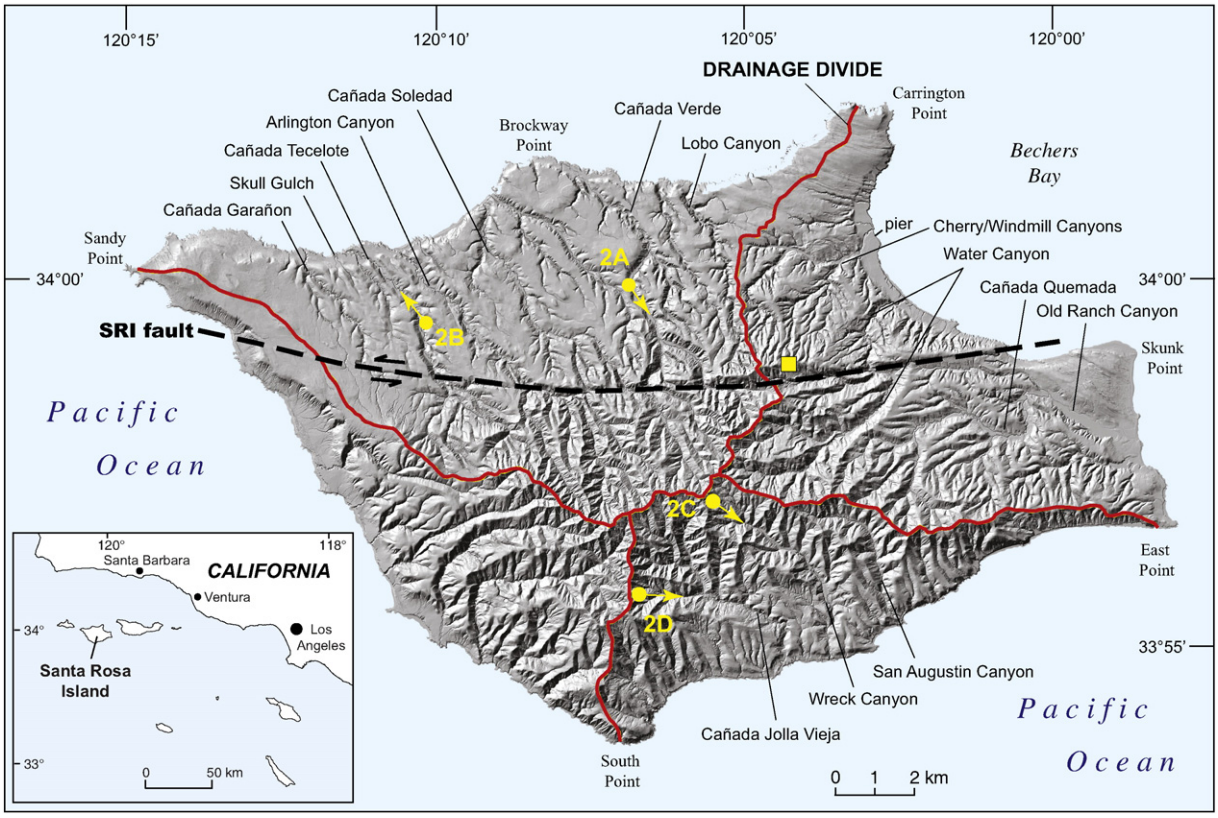

Fig. 1. Shaded relief map of Santa Rosa Island (SRI) showing names and locations of major drainages and place names. Yellow square indicates location of Black Mountain. Red line follows the island's drainage divides. Dashed black line depicts the Santa Rosa Island fault. Points labeled 2A–D indicate location and direction of photos in Fig. 2. Inset: Location of SRI with respect to the other Channel Islands and southern California mainland.

70 km west of Oxnard, CA. Santa Rosa Island is one of the five islands in Channel Islands National Park. The island has a maritime Mediterranean climate, with cool, rainy winters and warm, dry summers. Average annual precipitation is ~280 mm, with roughly 75% of the total falling in winter months (Dec–Mar) (Western Regional Climate Center, 2015). Air temperatures on the island rarely exceed 30 °C or fall below 10 °C. Modern plant communities include coastal sage scrub, island chaparral, grassland, and very sparse oak and pine woodlands (Junak et al., 2007).

During and following the last glacial period, the climate of the region was cooler and wetter, supporting an extensive coastal conifer forest of pine, fir, and cypress on adjacent Santa Cruz Island (Anderson et al., 2008) and probably also in the uplands of SRI. By about 11.8 ka, patchy pine woodlands, coastal sage scrub, and grasslands had replaced the forests as the climate warmed (Anderson et al., 2010). Further drying occurred during the early Holocene (~9–7 ka), after which a modest recovery was reflected in the reestablishment of grassland vegetation. Winter precipitation increased again slightly after ca. 4.5 ka, essentially establishing the modern climate conditions that persist today (Cole and Liu, 1994; Anderson et al., 2010).

Santa Rosa Island and the other three northern Channel Islands are the emergent parts of an ~125-km-long, uplifted anticlinal platform that, along with the Santa Monica Mountains to the east, form the southern part of the western Transverse Ranges crustal block (Crouch, 1979; Vedder and Howell, 1980). Approximately 2000 m of mostly marine shale, siltstone, sandstone, conglomerate, and volcaniclastic rocks of Eocene to Miocene age, with local volcanic flows and shallow intrusions, are exposed on Santa Rosa Island (Avila and Weaver, 1969; Weaver and Doerner, 1969; Dibblee and Eherenspeck, 1998). Most of the pre-Pleistocene rocks were deposited in shallow- to deep-water ocean environments that predated the island's emergence. Pleistocene and Holocene surficial deposits include colluvium and alluvium on the slopes and floors of valleys, eolian sand sheets and dunes, marine-terrace deposits (some of which form narrow coastal plains) and modern beach sands (Dibblee and Eherenspeck, 1998; Woolley, 1998). Landslides are common in many areas, particularly on steeper slopes in the southern and central parts of the island.

The island is bisected by the roughly east-west striking, subvertical to steeply north-dipping, Santa Rosa Island fault (SRIF; Fig. 1). Left-lateral strike-slip movement along the fault has caused the northern part of the island to move west, or left, relative to the southern part, giving Santa Rosa Island its distinctive, crudely parallelogram shape. Drainages that cross the fault are deflected as much as 1 km to the west on the north side of the fault, reflecting relatively recent (late Pleistocene and/or Holocene) lateral movement (Colson et al., 1995). Displacement of bedrock units suggests that the SRIF has also experienced vertical displacement, with rock units on the south side of the fault being displaced upward relative to the north side by as much as 400 m (e.g., Dibblee and Eherenspeck, 1998). North of the SRIF, the landscape is dominated by uplifted, early to middle Pleistocene marine terraces (Muhs et al., 2014) that form a relatively flat, gently seaward-sloping plain interrupted by the valleys of northwest-flowing streams. South of the fault, the topography is steeper, more rugged, and highly dissected. Because of the higher relative uplift on the south side of the fault, the island's drainage divide has also shifted southward (Fig. 1). Geomorphic evidence and orientations of striae along fault-slip surfaces suggest that more recent fault displacement caused relative uplift of the north side of the SRIF, particularly in the area around Black Mountain (Minor et al., 2012; Schumann et al., 2014). The SRIF is the only fault that crosses the entire island, although a number of secondary faults strike subparallel to the SRIF.

Some of the more striking landscape features on Santa Rosa Island are the incised alluvial valleys that characterize nearly all of the northward-draining streams, as well as a few large streams elsewhere on the island. These wide, trough-shaped valleys were filled with

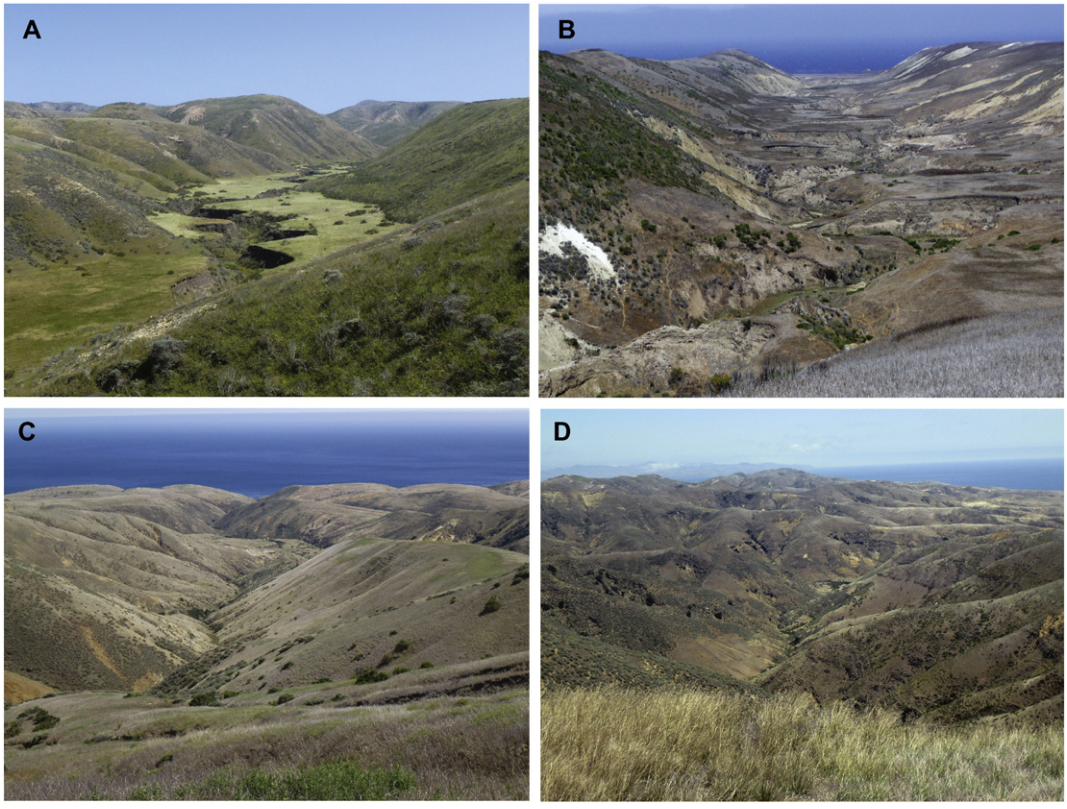

Fig. 2. Photos illustrating the contrast in morphology between drainages flowing north (A,B) and south (C,D) of the island's main drainage divide. (A) Cañada Verde. (B) Cañada Tecelote. (C) Wreck Canyon. (D) Cañada La Jolla Vieja.

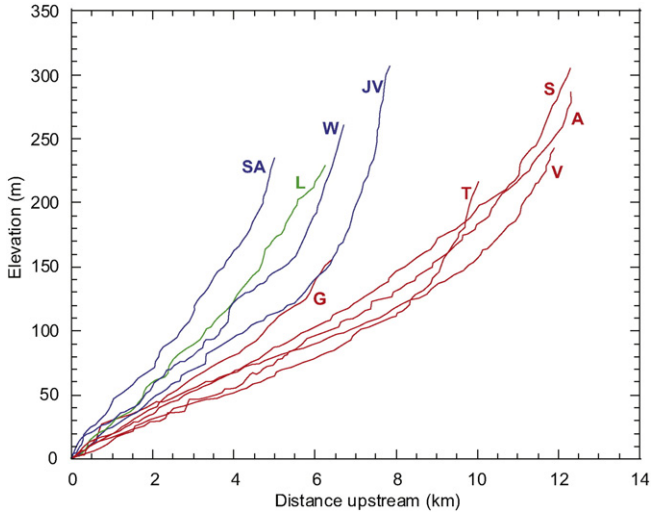

Fig. 3. Channel longitudinal profiles of major drainages on SRI. North-draining streams plotted in red, south-draining streams are in blue. Lobo Canyon, which drains north, is plotted in green. SA – San Augustin; L – Lobo; W – Wreck; JV – Jolla Vieja; G – Garañon; T – Tecelote; S – Soledad; A – Arlington; V – Verde.

alluvium and later incised to form steep- to vertical-walled arroyos, or barrancas, leaving a relict floodplain as much as 125 m wide and 10 or more meters above the active modern channel (Woolley, 1998). In many of the canyons, the alluvial fill exhibits a distinctive sequence of alternating lighter and darker beds. The physical character of these drainage systems and their sediments, what they may indicate regarding the response of the island's fluvial systems to the extreme lowering of sea level at the Last Glacial Maximum (LGM), and how they responded to the subsequent return of sea level to its present elevation during the late Pleistocene and Holocene are the focal points of this study.

3. Field and laboratory methods

Exposures of alluvial fill in several canyons on SRI were investigated during multiple visits to the island between 2012 and 2015. The location of each station was accurately determined by Global Positioning System (GPS); and the section was measured, photographed, sketched, and described. Samples of bulk sediment were collected from selected horizons for radiocarbon dating or determination of physical properties. In many locations, discrete fragments of charcoal or shells of the San Miguel Shoulderband snail (*Helminthoglypta ayresiana*) were collected for radiocarbon age determination.

Sediment, charcoal, and snail shell samples were submitted to the U.S. Geological Survey's radiocarbon laboratory in Reston, Virginia, for radiocarbon (^{14}C) dating, except samples Cv52-2 and CV52-4, which were analyzed by Aeon Laboratories, LLC. Charcoal samples were subjected to a standard acid-base-acid (ABA) treatment and were combusted to CO_2 under vacuum in the presence of CuO and Ag. Humic acids were collected as the base-soluble fraction of the sample material, filtered through a 0.45-μm Metricel membrane filter, and then acidified in 1 M HCl. The precipitated humic acids were then neutralized in ultrapure water, isolated by centrifuge, dried in an oven overnight at 70 °C, and combusted as above. Snail shells were separated from the host sediment, placed in a beaker of ASTM Type 1, 18.2 MW (ultrapure) water, and subjected to an ultrasonic bath for a few seconds. The shells were then repeatedly immersed in a second beaker of ultrapure water to remove material adhering to the shell surface or lodged within the shell itself. This process was repeated until the shells were visibly clean. The shells were then treated in 3% H_2O_2 for 24 h at room temperature to remove all remnants of organic matter. Finally, the shells were washed repeatedly in ultrapure water and dried in an oven overnight at 70 °C. After cleaning, the shells were converted to

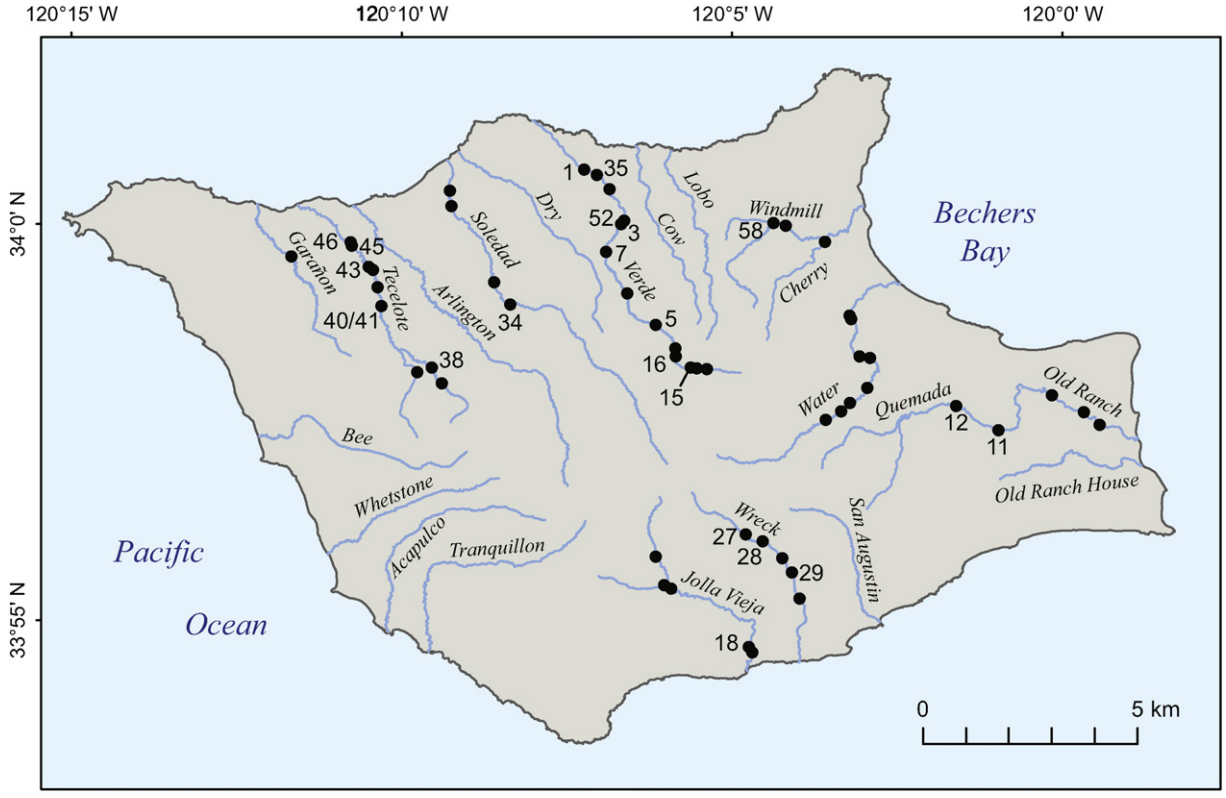

Fig. 4. Map showing locations of alluvial sections measured, described, and sampled in this study. Numbers correspond to ^{14}C-dated sections (Table 2) or to sections otherwise mentioned in text.

Table 1
Station location information.

Station #	Latitude (°N)	Longitude (°W)	Elevation (m)	Dated by ^{14}C?
Cherry Canyon				
CC-56	34.0010	120.0584	33	N
Cañada Garañon				
GC-51	33.9945	120.1927	36	N
Cañada La Jolla Vieja				
JV-17	33.9143	120.0736	41	N
JV-18	33.9153	120.0744	28	Y
JV-19	33.9271	120.0944	34	N
JV-20	33.9278	120.0961	124	N
JV-21	33.9338	120.0986	121	N
Old Ranch Canyon				
ORC-53	33.9643	119.9876	4	N
ORC-54	33.9668	119.9917	9	N
ORC-55	33.9702	119.9999	15	N
Quemada Canyon				
QC-11	33.9625	120.0131	52	Y
QC-12	33.9673	120.0239	72	Y
Cañada Soledad				
CS-08	33.9904	120.1414	70	N
CS-09	34.0093	120.1532	39	N
CS-10	34.0062	120.1527	40	N
CS-34	33.9859	120.1371	79	Y
Cañada Tecelote				
TC-37	33.9688	120.1538	111	N
TC-38	33.9721	120.1564	96	Y
TC-39	33.9710	120.1601	98	N
TC-40/41[a]	33.9847	120.1696	56	Y
TC-42	33.9886	120.1708	52	N
TC-43	33.9928	120.1731	38	Y
TC-44	33.9922	120.1720	39	N
TC-45	33.9972	120.1775	31	Y
TC-46	33.9978	120.1779	32	Y
Cañada Verde				
CV-01	34.0147	120.1195	26	Y
CV-02	34.0107	120.1130	50	Y
CV-03	34.0034	120.1099	60	Y
CV-04	33.9776	120.0952	136	N
CV-05	33.9825	120.1003	121	Y
CV-06	33.9890	120.1078	106	N
CV-07	33.9975	120.1134	78	Y
CV-13	33.9735	120.0871	183	N
CV-14	33.9736	120.0896	170	N
CV-15	33.9737	120.0911	159	Y
CV-16	33.9759	120.0950	151	N
CV-35	34.0136	120.1163	119	Y
CV-52	34.0042	120.1091	49	Y
Water Canyon				
WC-22	33.9636	120.0568	125	N
WC-23	33.9655	120.0530	116	N
WC-24	33.9673	120.0507	125	N
WC-25	33.9706	120.0465	99	N
WC-26	33.9771	120.0487	76	N
WC-31	33.9849	120.0511	45	N
WC-32	33.9769	120.0460	63	N
WC-33	33.9857	120.0515	37	N
Windmill Canyon				
WMC-57	34.0041	120.0683	57	N
WMC-58	34.0046	120.0714	64	Y
Wreck Canyon				
RC-27	33.9390	120.0761	104	Y
RC-28	33.9376	120.0717	120	Y
RC-29	33.9313	120.0642	70	Y
RC-30	33.9258	120.0620	61	N
RC-36	33.9342	120.0667	82	N

[a] Stations TC-40 and TC-41 were located ~10 m apart on opposite sides of an active wash.

CO_2 using ACS reagent grade, 85% H_3PO_4 under vacuum at 50 °C, for ~1 h, until the reaction was visibly complete.

Sample CO_2 was converted to graphite using an Fe catalyst and a standard hydrogen reduction process. Graphite samples were pressed into targets and submitted to the Center for Accelerator Mass Spectrometry (CAMS) at Lawrence Livermore National Laboratory for ^{14}C analysis. For most samples, a second aliquot of CO_2 was isolated and submitted to the Stable Isotope Laboratory, University of California, Davis, for $\delta^{13}C$ analysis in order to correct the measured ^{14}C activity of the samples for isotopic fractionation. All ^{14}C ages were calibrated using the IntCal13 data set and CALIB 7.1 (Stuiver and Reimer, 1993; Reimer et al., 2013). Ages from this study are presented in thousands of calibrated ^{14}C YBP (Years Before Present; 0 YBP = 1950 CE; ka = thousands of calibrated ^{14}C YBP), and uncertainties are given at the 95% (2σ) confidence level. Ages from other sources are reported as published. Bacon statistical age-depth modeling software (Blaauw and Christen, 2011) was used to model age-depth relationships of the alluvial sediments and to extrapolate an estimated age of alluvium at the base (modern stream level, assumed to be at or very near the bedrock valley floor) of the alluvial deposit at each section.

Samples of alluvial sediments from Cañada Verde were also analyzed for particle-size distribution and organic content. The sediment samples were passed through a 2-mm sieve to remove gravel and larger particles, then prepared by digesting organic matter and $CaCO_3$ using 30% H_2O_2 and 10% HCl, respectively. When required, $(NaPO_3)_6$ was added to each sample as a clay dispersant. The samples were then analyzed using a Malvern Masterizer 2000 laser particle size analyzer in the USGS soils laboratory in Denver, CO.

Total organic matter content of sediment samples was determined from loss on ignition (LOI) by the Colorado State University Soil, Water, and Plant Testing Laboratory in Fort Collins, CO. The samples were dried in an oven at 90–100 °C for 1 h, then weighed. The samples were then heated to 550 °C for 1 h and weighed again. The difference in the two masses, expressed in percent, represents the amount of organic carbon lost from the samples during combustion (Dean, 1974).

Digital representations of the topography and river long profiles were extracted from a 1-m resolution, LiDAR-based digital elevation model (DEM) of the Channel Islands (USGS Channel Islands ARRA LiDAR Project). Bathymetry data for the northern Channel Islands platform are from the National Oceanic and Atmospheric Administration's (NOAA) Coastal Inundation Project (Carignan et al., 2009). Data from both sources were processed with Environmental Systems Research Institute's ArcGIS software to develop shaded relief images of topography. ArcHydro tools were used within ArcGIS to infer drainages from the DEM data and extract distance-elevation data for stream profiles.

4. Results

The shapes and configurations of the river valleys on Santa Rosa Island are largely a result of fluvial dissection of landscapes created by tectonic and eustatic processes. North of the Santa Rosa Island fault, the upland surfaces of the island are the remnants of uplifted marine terraces, and the interfluves are broad, relatively flat, and gently seaward sloping. The major drainages on this side of the island trend to the northwest, and the valleys are relatively broad, with a trough-like appearance, containing remnants of alluvial fill in the form of narrow to broad alluvial terraces that typically stand 2–14 m above the present stream channels (Fig. 2A, B). South of the SRIF, the relief is greater, the valleys are generally deeper and more V-shaped, and the interfluves are typically narrow ridges (Fig. 2C, D). Most of the bedrock valleys in the southern part of the island also contain alluvial fill, but the terraces, where present, are discontinuous and are only found in wider sections of the valley. The north- and south-draining streams also exhibit different channel longitudinal profiles (Fig. 3). The south-draining streams are shorter in overall length because of the southward offset of the island's drainage divide, and have steeper gradients than the north-

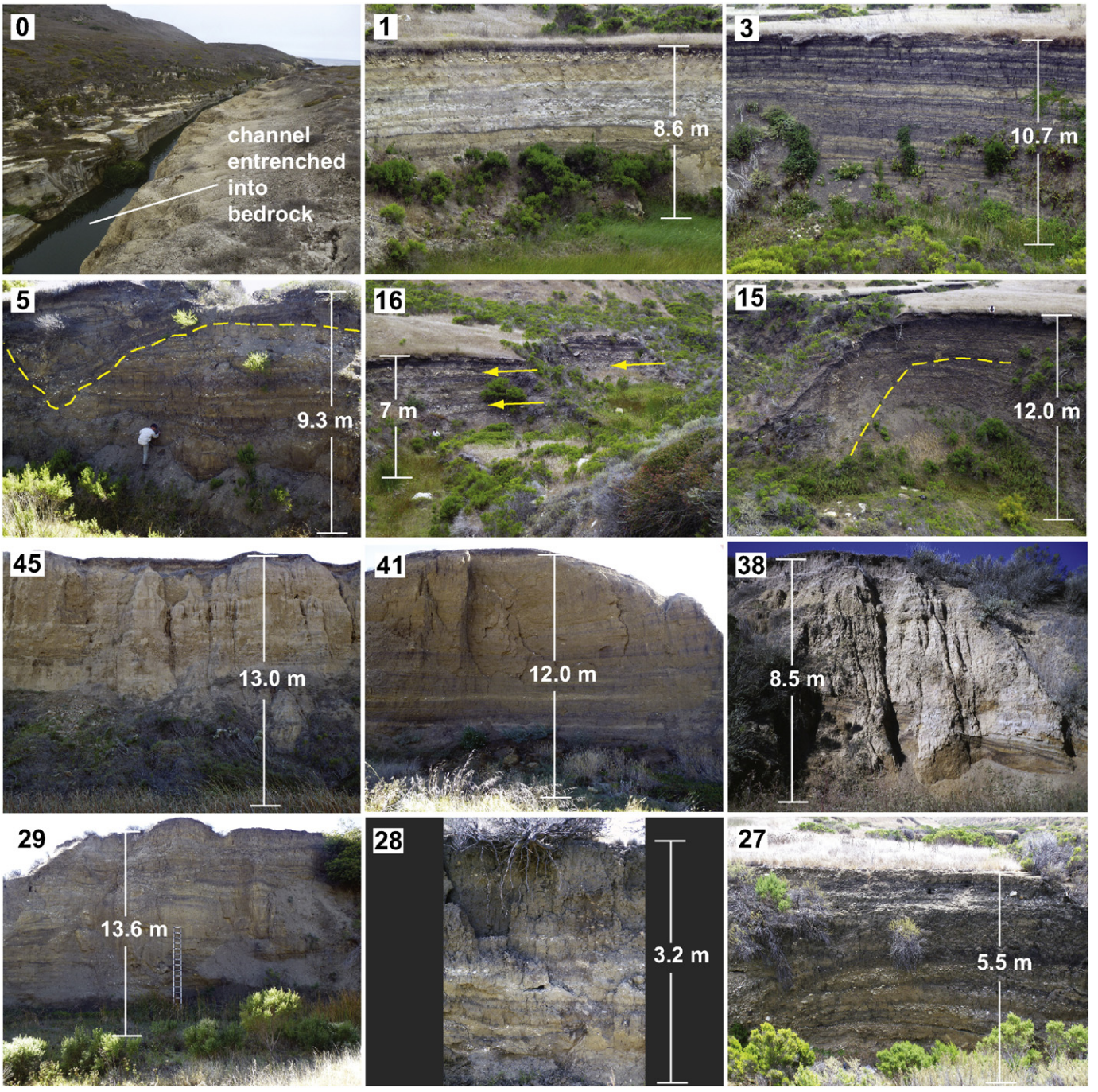

Fig. 5. Photos of alluvial sections in Cañada Verde, Cañada Tecelote, and Wreck Canyon. Photos for each canyon are presented in order, proceeding upstream. Except for photo 0, numbers on photos indicate the station number, keyed to locations shown on Fig. 4. Photo 0 taken ~1.5 km downstream of station 1, near the mouth of Cañada Verde at the coast. At this location, the channel has incised into sandstone bedrock. The incision likely happened during a period of low sea level. At stations 5 and 15, the dashed yellow line follows erosional base of channel fill. At station 16, note coarse-grained colluvium interbedded with floodplain alluvium (yellow arrows).

draining streams. A standout exception to this pattern is Lobo Canyon, which is in the north, but plots in the grouping with the southward-draining streams (L, Fig. 3). Lobo Canyon heads at Black Mountain in an area thought to be experiencing recent tectonic uplift associated with the SRIF (Minor et al., 2012; Schumann et al., 2014). Also unlike the other northward-draining streams, Lobo Canyon is mostly devoid of alluvial fill, except in its lowest ~0.5 km, in which only sparse, eroded remnants of alluvial terraces remain. Thus, Lobo Canyon resembles the south-draining stream systems more than the adjacent north-draining streams.

We examined 54 exposures of alluvial fill in 10 canyons on SRI between 2012 and 2015 (Fig. 4, Table 1). These drainages contain alluvial deposits ranging from ~2 to ~14 m thick, into which arroyos have been incised and through which the modern streams flow (Fig. 2). In most places, the modern streams appear to be flowing on the bedrock valley floor surface or on a thin (typically <0.5 m) veneer of modern alluvium. The alluvial terrace deposits typically consist of horizontal to subhorizontal, alternating lighter and darker beds of sediment of varying thickness, with occasional beds or lenses of gravel or cobbles (Fig. 5). The darker beds generally contain silty clay or clay and organic

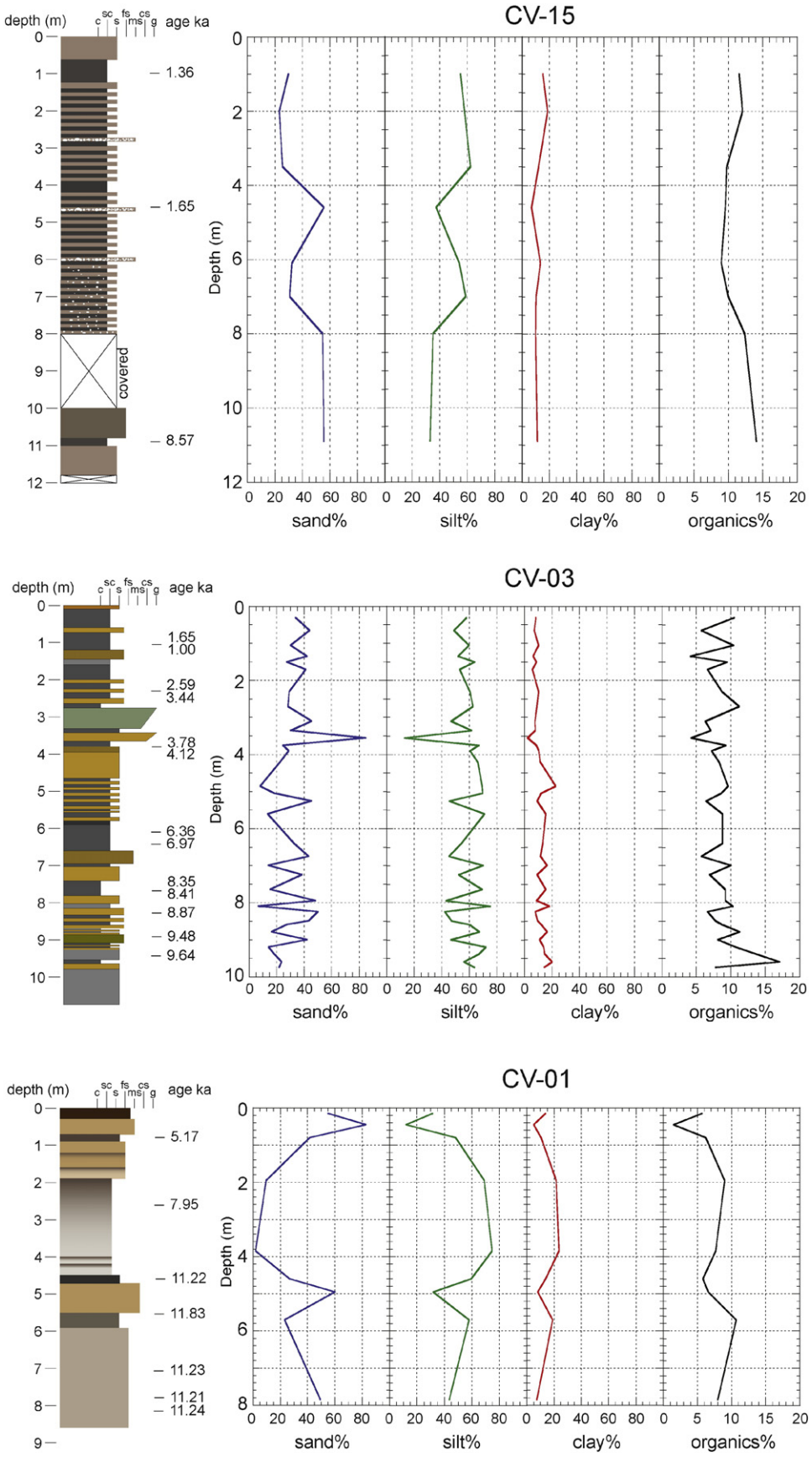

Fig. 6. Sedimentary sections, calibrated ages, particle-size data, and organic content of sediments for three sections in Cañada Verde. Colors approximate actual color of sediments. Length of bars indicate dominant grain size of each unit ranging from clay (c) to gravel (g).

Table 2
Summary of AMS sample information, carbon-14 ages, and calibrated ages.[a]

Sample #	Lab #[b]	AMS #	Station	Material dated[c]	Depth (m)[d]	$\delta^{13}C$ (‰ vpdb)[e]	^{14}C age (^{14}C ka BP)	Intercept 1 Age (cal ka BP)[f]	P[g]	Intercept 2 Age (cal ka BP)[f]	P[g]	Intercept 3 Age (cal ka BP)[f]	P[g]	Median age (cal ka BP)[h]
Cañada La Jolla Vieja														
JV18-1a	WW-9874	CAMS-166416	18	shell	0.95	−4.3	1.30±0.04	1.24±0.06	1.00					1.24
Quemada Canyon														
QC11-8	WW-9425	CAMS-161484	11	humic acids	1.75	−25.6	0.95±0.03	0.86±0.06	1.00					0.85
QC11-7	WW-9194	CAMS-159705	11	charcoal	2.60	−25.4	1.14±0.03	1.03±0.06	0.88	1.13±0.02	0.08			1.03
QC11-7	WW-9273	CAMS-160270	11	humic acids	2.60	−25.3	1.08±0.03	0.97±0.04	0.73	1.04±0.02	0.27			0.98
QC11-3	WW-9271	CAMS-160280	11	charcoal	3.15	−25	1.06±0.04	0.97±0.04	0.84	1.04±0.02	0.16			0.96
QC11-4	WW-9193	CAMS-159703	11	charcoal	4.20	−22.3	1.31±0.03	1.20±0.01	0.28	1.26±0.04	0.72			1.25
QC11-4	WW-9308	CAMS-160421	11	humic acids	4.20	−25	1.59±0.04	1.48±0.08	1.00					1.47
QC11-1	WW-9192	CAMS-159702	11	charcoal	4.30	−27.0	1.19±0.03	1.12±0.06	0.98					1.12
QC11-1	WW-9272	CAMS-160281	11	humic acids	4.30	−26.3	1.45±0.03	1.34±0.04	1.00					1.34
QC12-2	WW-9885	CAMS-166429	12	charcoal	4.75	−26.3	9.57±0.03	10.81±0.07	0.45	11.00±0.08	0.55			10.95
Cañada Soledad														
SC34-B170	WW-9922	CAMS-167390	34	humic acids	1.50	−25.5	1.19±0.03	1.12±0.06	0.98					1.12
SC34-1	WW-9884	CAMS-166428	34	charcoal	4.50	−25.5	8.60±0.03	9.57±0.05	1.00					9.55
Cañada Tecelote														
TC38-1	WW-9883	CAMS-166427	38	charcoal	9.00	−25.1	12.19±0.03	14.08±0.11	1.00					14.08
TC40-1	WW-9881	CAMS-166425	40	shell	9.20	−8.3	10.57±0.03	12.6±0.04	0.25	12.58±0.06	0.75			12.55
TC41-10	WW-10167	CAMS-168755	41	charcoal	8.85	−25	11.15±0.04	13.02±0.09	1.00					13.04
TC41-9	WW-10101	CAMS-168388	41	charcoal	9.60	−23.5	12.50±0.05	14.69±0.36	1.00					14.72
TC41-5	WW-10179	CAMS-168767	41	charcoal	10.10	−25	9.65±0.04	10.88±0.09	0.47	11.13±0.06	0.51			11.04
TC41-6	WW-10100	CAMS-168387	41	charcoal	10.74	−24.0	10.92±0.03	12.77±0.06	1.00					12.77
TC41-7	WW-10102	CAMS-168389	41	charcoal	11.04	−22.7	10.77±0.03	12.70±0.04	1.00					12.70
TC41-1	WW-9882	CAMS-166426	41	charcoal	11.25	−25.2	10.94±0.03	12.78±0.06	1.00					12.77
TC43-1	WW-9760	CAMS-165479	43	Physa shell	0.70	−1.7	0.36±0.03	0.36±0.04	0.48	0.46±0.04	0.52			0.43
TC43-4	WW-9761	CAMS-165480	43	shell	4.05	−7.9	0.77±0.03	0.70±0.03	1.00					0.69
TC45-4	WW-10085	CAMS-168374	45	shell	3.80	−10.8	8.84±0.03	9.86±0.10	0.59	10.01±0.03	0.09	10.10±0.05	0.32	9.92
TC45-3	WW-9763	CAMS-165482	45	shell	5.30	−9.8	9.96±0.03	11.33±0.08	0.84	11.46±0.03	0.08	11.57±0.03	0.08	11.35
TC45-2	WW-9762	CAMS-165481	45	shell	5.80	−9.1	10.03±0.03	11.49±0.16	0.93	11.69±0.02	0.07			11.51
TC46-1	WW-10170	CAMS-168758	46	charcoal	4.25	−25	13.33±0.04	16.02±0.18	1.00					16.03
TC46-2	WW-10172	CAMS-168760	46	humic acid	4.80	−24.1	13.57±0.03	16.36±0.17	1.00					16.34
Cañada Verde														
CV1-B6	WW-9779	CAMS-165497	1	bulk organics	0.80	−19.3	4.50±0.03	5.12±0.08	0.65	5.25±0.04	0.35			5.17
CV1-10	WW-9875	CAMS-166417	1	shell	2.60	−10.6	7.11±0.03	7.88±0.02	0.18	7.95±0.03	0.82			7.95
CV1-B4	WW-9778	CAMS-165496	1	bulk organics	4.60	−25.0	9.80±0.04	11.22±0.03	1.00					11.22
CV1-4	WW-9889	CAMS-166433	1	charcoal	5.55	−23.8	10.15±0.04	11.86±0.16	0.95					11.83
CV1-9	WW-9890	CAMS-166434	1	charcoal	7.05	−25.7	9.83±0.03	11.23±0.02	1.00					11.23
CV1-2	WW-9964	CAMS-167494	1	charcoal	7.78	−25	9.77±0.03	11.20±0.03	1.00					11.21
CV1-8	WW-9965	CAMS-167495	1	charcoal	8.16	−25	9.84±0.03	11.23±0.03	1.00					11.24
CV2-1	WW-9423	CAMS-161482	2	humic acids	1.45	−24.9	9.22±0.04	10.35±0.09	0.86	10.47±0.02	0.14			10.37
CV52-1[i]	WW-10491	CAMS-171266	52	charcoal	9.10	−25	8.32±0.04	9.35±0.11	0.95					9.35
CV52-2[i,j]	P-1519A	Aeon-2111	52	conc organics	10.05	−25	9.80±0.05	11.22±0.06	1.00					11.22
CV52-4[i,j]	P-1519C	Aeon-2113	52	conc organics	11.80	−25	11.27±0.05	13.15±0.10	1.00					13.13
CV3-B38	WW-9395	CAMS-161188	3	humic acids	1.05	−25.5	1.74±0.03	1.58±0.01	0.06	1.65±0.06	0.94			1.65
CV3-12	WW-9382	CAMS-161173	3	shell	1.06	−8	1.10±0.04	1.00±0.07	1.00					1.00

(continued on next page)

Table 2*(continued)*

Sample #	Lab #[b]	AMS #	Station	Material dated[c]	Depth (m)[d]	$\delta^{13}C$ (‰ vpdb)[e]	^{14}C age (^{14}C ka BP)	Intercept 1 Age (cal ka BP)[f]	P[g]	Intercept 2 Age (cal ka BP)[f]	P[g]	Intercept 3 Age (cal ka BP)[f]	P[g]	Median age (cal ka BP)[h]
CV3-9	WW-9381	CAMS-161172	3	shell	2.30	−8.6	2.50 ± 0.03	2.61 ± 0.12	1.00					2.59
CV3-B34	WW-9394	CAMS-161187	3	humic acids	2.30	−25.7	3.23 ± 0.03	3.43 ± 0.05	0.97					3.44
CV3-B29	WW-9393	CAMS-161186	3	humic acids	3.75	−25.6	3.76 ± 0.03	4.02 ± 0.02	0.09	4.12 ± 0.04	0.76	4.21 ± 0.02	0.11	4.12
CV3-7	WW-9380	CAMS-161171	3	shell	3.80	−7.1	3.52 ± 0.03	3.79 ± 0.09	1.00					3.78
CV3-4	WW-9379	CAMS-161170	3	shell	6.10	−9.4	5.60 ± 0.03	6.36 ± 0.05	0.99					6.36
CV3-B23	WW-9392	CAMS-161185	3	humic acids	6.40	−25.7	6.11 ± 0.03	6.96 ± 0.07	0.90	7.13 ± 0.02	0.10			6.97
CV3 -B19	WW-9391	CAMS-161184	3	humic acids	7.64	−26.1	7.51 ± 0.03	8.24 ± 0.02	0.11	8.35 ± 0.05	0.89			8.35
CV3-3	WW-9378	CAMS-161169	3	shell	7.67	−9.5	7.62 ± 0.03	8.41 ± 0.03	1.00					8.41
CV3-16	WW-9764	CAMS-165483	3	shell	8.26	−8.9	7.98 ± 0.03	8.86 ± 0.14	1.00					8.87
CV3-19	WW-9765	CAMS-165484	3	shell	8.93	−9.1	8.45 ± 0.04	9.48 ± 0.05	1.00					9.48
CV3-21	WW-9766	CAMS-165485	3	shell	9.44	−13.6	8.71 ± 0.03	9.64 ± 0.09	1.00					9.64
CV5-B44	WW-9887	CAMS-166431	5	bulk organics	1.80	−25.2	0.93 ± 0.03	0.85 ± 0.06	1.00					0.85
CV5-B174	WW-9891	CAMS-166435	5	bulk organics	2.20	−24.3	5.17 ± 0.03	5.92 ± 0.03	0.85	5.98 ± 0.01	0.15			5.92
CV5-B174	WW-9915	CAMS-167383	5	humic acids	2.20	−25.0	5.31 ± 0.03	6.09 ± 0.09	1.00					6.09
CV5-1	WW-9424	CAMS-161483	5	humic acids	5.20	−24.6	6.67 ± 0.03	7.54 ± 0.05	1.00					7.54
CV5-B41	WW-9923	CAMS-167391	5	humic acids	6.73	−25.7	7.62 ± 0.03	8.41 ± 0.03	1.00					8.41
CV7-2	WW-9196	CAMS-159707	7	charcoal	5.95	−25.9	4.49 ± 0.03	5.16 ± 0.12	1.00					5.18
CV7-2	WW-9270	CAMS-160279	7	humic acids	5.95	−25	4.41 ± 0.03	4.96 ± 0.09	0.95					4.98
CV15-B119	WW-10003	CAMS-167751	15	bulk organics	1.00	−25.3	1.47 ± 0.03	1.36 ± 0.05	1.00					1.36
CV15-1	WW-9886	CAMS-166430	15	discrete organics	4.60	−23.5	1.74 ± 0.03	1.58 ± 0.01	0.06	1.65 ± 0.06	0.94			1.65
CV15-B120	WW-9780	CAMS-165498	15	bulk organics	10.90	−25	7.79 ± 0.04	8.48 ± 0.02	0.10	8.57 ± 0.06	0.90			8.57
CV35-B178	WW-9920	CAMS-167388	35	humic acids	0.90	−26.6	0.48 ± 0.03	0.52 ± 0.02	1.00					0.52
CV35-B178	WW-9921	CAMS-167389	35	bulk organics	0.90	−26.7	0.54 ± 0.03	0.54 ± 0.02	0.81	0.62 ± 0.01	0.19			0.54
CV35-1	WW-9873	CAMS-166415	35	shell	3.35	−9.9	6.99 ± 0.04	7.80 ± 0.08	0.81	7.91 ± 0.02	0.19			7.83
Windmill Canyon														
WMC58-1	WW-10487	CAMS-171262	58	charcoal	2.00	−23.9	2.26 ± 0.04	2.21 ± 0.06	0.65	2.32 ± 0.03	0.35			2.24
Wreck Canyon														
RC27-B153b	WW-9892	CAMS-166436	27	humic acids	0.30	−25.7	0.51 ± 0.03	0.53 ± 0.02	1.00					0.53
RC27-B153a	WW-9888	CAMS-166432	27	bulk organics	0.30	−25.7	0.68 ± 0.03	0.58 ± 0.01	0.33	0.66 ± 0.02	0.67			0.66
RC27-B152	WW-9917	CAMS-167385	27	humic acids	2.20	−25.7	2.24 ± 0.03	2.21 ± 0.06	0.75	2.32 ± 0.02	0.25			2.23
RC27-1	WW-9876	CAMS-166420	27	shell	4.20	−7.0	4.69 ± 0.03	5.37 ± 0.05	0.66	5.45 ± 0.02	0.23	5.56 ± 0.02	0.10	5.40
RC28-B157	WW-9919	CAMS-167387	28	humic acids	0.30	−25.5	1.63 ± 0.03	1.44 ± 0.02	0.23	1.54 ± 0.03	0.69			1.54
RC28-2b	WW-9878	CAMS-166422	28	shell	2.70	2.7	3.41 ± 0.03	3.64 ± 0.06	1.00					3.65
RC28-1b	WW-9877	CAMS-166421	28	shell	3.10	1.2	3.39 ± 0.04			3.64 ± 0.08	0.99			3.63
RC29-B180	WW-9918	CAMS-167386	29	humic acids	0.90	−24.9	1.53 ± 0.03	1.39 ± 0.04	0.64	1.49 ± 0.03	0.34			1.41
RC29-1	WW-9916	CAMS-167384	29	humic acids	4.50	−24.8	2.85 ± 0.03	2.95 ± 0.08	0.99					2.95
RC29-3	WW-9879	CAMS-166423	29	shell	8.40	−6.9	4.78 ± 0.03	5.52 ± 0.04	0.85	5.58 ± 0.01	0.15			5.52
RC29-4	WW-9880	CAMS-166424	29	shell	9.70	−8.0	4.72 ± 0.03	5.37 ± 0.04	0.49	5.46 ± 0.02	0.22	5.55 ± 0.03	0.29	5.45
RC29-2	WW-9781	CAMS-165499	29	charcoal	11.95	−26.7	7.52 ± 0.04	8.24 ± 0.02	0.10	8.35 ± 0.05	0.90			8.35

[a] Uncertainties for the calibrated ages are given at the 2σ (95%) confidence level. All other uncertainties are presented at 1σ (68%).
[b] WW = USGS Radiocarbon Laboratory, Reston VA; P = USGS Desert Research Laboratory, Denver CO.
[c] shell = *Helminthoglypta ayersiana*; bulk/discrete organics refers to the base-insoluble fraction of the organic matter; humic acids refers to the base-soluble fraction.
[d] Depth from top of exposure.
[e] Data reported for δ13C with a single decimal place represent measured values. Those without decimal places are assumed values.
[f] Calibrated ages were calculated using CALIB v.7.1 in conjunction with the IntCal13.14C dataset; limit 50 ka cal BP. Calibrated ages are reported as the midpoint of the calibrated range. Uncertainties are reported as the difference between the midpoint and either the upper or lower limit of the calibrated age range, whichever is greater. Ages are reported when the probability of a calibrated age range exceeds 0.05.
[g] P = probability of the calibrated age falling within the reported range as calculated by CALIB.
[h] Median age as calculated by CALIB.
[i] Same stratigraphic section as Pinter et al. (2011). Sample CV52-1 was taken from approximately the same depth as their sample #SRI-07-P3.
[j] Following the initial acid step, these samples were treated at the USGS Desert Research Laboratory with HF and HCl to remove silicates and concentrate organic material. The samples were then submitted to Aeon Laboratories, LLC and treated in an identical manner to the others with the exception that combustion of the concentrated organic material was done online.

matter, whereas the lighter-colored beds are composed primarily of silt and sand and do not contain as much organic matter. The darker sediments appear to represent floodplain paleosols that developed during relatively stable and (or) wetter periods, when lush grasses or wetlands covered the floodplains, or perhaps organic-rich, low-energy channel sediments. The lighter sediments are interpreted as channel-margin or floodplain aggradational deposits. Channel-fill sequences containing sand and gravel are locally found cutting into the floodplain deposits (Fig. 5, stations 5, 15).

Some discrete beds can be traced up- or downstream for hundreds of meters, whereas in other locations the sedimentary sequences appear to be quite localized in lateral extent. Sediments with more continuity in the up/downstream direction tend to be horizontally bedded, suggesting longer downstream transport distances. Beds that are dipping toward the center of the valley suggest more localized contribution of sediment from valley side slopes or from tributary drainages, probably with shorter downstream transport distances. Proximal to valley walls (or where the valleys are relatively narrow) gravel, cobbles, and boulders of bedrock from slope wash and mass movements form lenses or beds of colluvium that may be mixed with the axial alluvial sediments (Fig. 5, station 16).

Plots of particle size and organic content of sediments for three sections in Cañada Verde illustrate the episodic deposition of the alluvial deposits and display an inverse relationship between sand and silt content in sediments (Fig. 6). The proportion of clay generally varies between 0 and 20%, and clay content roughly follows silt content in sediments. The alluvium also contains 5–15% organic matter, with higher concentrations of organics in the darker-colored, finer-grained sediments (Fig. 6), strongly suggesting that the darker shades of the sediments are related to the presence and abundance of organic material, in contrast to the findings of Pinter et al. (2011). There appears to be a very slight overall coarsening of sediments in the downstream direction, with a corresponding slight decrease in organic content (Fig. 6). This is contrary to the expected downstream fining of sediments and may be caused by input from local landslides and slopewash that are relatively common along the valley walls (Fig. 5, station 16). Such activities would contribute coarse sediment to the alluvium along the length of the canyon, partially negating the stream's downstream sorting processes. We did not analyze sediments from other drainages for particle size and organic content, so we were unable to determine if this trend applies to other drainages on the island, or if the observed trend is related solely to fluvial processes, contributions of coarser sediment from valley side slopes and tributaries, differences in the bedrock source of sediment, or other factors.

Calibrated ^{14}C ages obtained from charcoals, humic acids, plant material, and terrestrial gastropod shells are given in Table 2. Except for several late Pleistocene samples from Cañada Tecelote, the alluvium ranges from early to late Holocene in age. In sections lacking obvious unconformities such as channel fills, the ^{14}C ages of samples generally increase with increasing depth, within the ranges of analytical uncertainties.

We analyzed a subset of the total suite of samples collected, focusing primarily on three canyons with well-expressed sedimentary records: Verde and Tecelote Canyons, which drain to the north, and Wreck Canyon, which drains to the south coast of the island (Figs. 4 and 5). The estimated age of the base of each alluvial deposit (Fig. 7) should indicate the time at which aggradation began at that location. At station TC41, the samples were collected in a relatively narrow range of depths and the ages do not linearly increase with depth, so the oldest of the samples (14.72 ka) was chosen to represent the estimated age of the base of the deposit. Likewise, at station TC38, only one sample was dated, and it is within 25 cm of the base of the deposit; its age was used as the estimated basal age. The age-depth curve for station CV5 is interrupted by a cut-and-fill channel sequence at ~200 cm depth (Fig. 5), but below the erosional unconformity, the rate of sediment accumulation appears to have been relatively constant (Fig. 7). Sample CV15-1 (Table 2) was collected within a channel fill deposit (Fig. 5) and did not form part of a continuous depositional sequence, so it was excluded from the age-depth plot (Fig. 7).

Vertical aggradation rates can be inferred from the sediment data at each exposure. An average sediment accumulation rate was calculated by dividing the vertical distance between the youngest and oldest samples at each location by the difference in age of the samples. Observed vertical sediment accumulation rates range from 60 to nearly 200 cm ka^{-1}. Where the age-depth curves presented in Fig. 7 are relatively linear, we assume that the aggradation rate was, on average, relatively constant, and that rapid, short-duration depositional or erosional events are not discernible within the resolution of sampling. However, the multiple depositional sequences at each section suggest that episodic, not continuous, aggradation built the floodplains. The varying thickness of aggradational sequences implies that the flood events were of varying magnitudes. The varying degree of paleosol development at the top of each sequence further suggests that the time period between overbank floods was also variable. Thus over the short term (tens to hundreds of years), floodplain aggradation rates would be expected to vary greatly. Over longer time intervals (thousands of years), however, the vertical aggradation rates appear to have been surprisingly constant (Fig. 7). For example, stations CV3, RC29, and TC45/46 have long sedimentary records interpreted from multiple samples. At each of these stations, a straight (or nearly straight) line can be fitted to the age-depth data (Fig. 7), indicating long-term consistency of vertical aggradation rates. No obvious erosion surfaces or unconformities were noted within these sections, although station 45/46 is a composite of two nearby sections.

At station CV1, the rate was calculated only for the upper ~400 cm, below which there appears to be an unconformity that is visible in the field and also indicated by a change in slope of the age-depth plot (Fig. 7). Below about 400 cm, all of the ages are very similar regardless of depth, suggesting that a rapid depositional event took place between about 12 and 11 ka at that location. At stations TC38 and TC41, the aggradation rate calculation is based on the depth and age of the oldest (or only) sample and assumes that the upper surface of the alluvium is modern, with negligible erosion. At these two locations, the aggradation rates should be considered minima.

Plots of the estimated maximum age of each alluvial section against distance of each section upstream from the river's mouth at the coastline show trends of decreasing age with distance upstream (Fig. 8). Linear regressions were fitted to the data in order to identify and quantify trends; however, the regressions are based on only 3–4 points each, insufficient to confirm that the relationships are indeed linear. In fact, the age-distance relationships may be considerably more complex. Nevertheless, the relatively good fit of simple regression lines to the data facilitates comparing trends between drainages and allows more informed speculation about the interaction and timing of sea-level rise and alluvial backfilling. The slope of the lines indicates the rate at which backfilling of sediment progressed upstream—the steeper the slope, the more slowly the wave of aggradation progressed upstream. It would be logical to expect that the rate of backfilling is related to physical characteristics of the drainages, one of the most obvious being channel gradient. Indeed, Cañada Verde, which has the lowest overall channel gradient of the three drainages plotted in Fig. 8, backfilled more rapidly than Tecelote Canyon, which has a slightly steeper gradient (Fig. 3). Wreck Canyon, with the steepest channel gradient of the three (Fig. 3), backfilled most slowly (Fig. 8). Local variations in gradient and valley morphology, or obstructions in the channel such as bedrock outcrops, would also affect the progression of sediment backfilling upstream. Assuming that all sediment was transported downstream until it reached the advancing edge of the aggradational wedge, the location and age of sediment at the base of each alluvial section may document the progression of backfilling in each canyon (Fig. 8). Extending the regression lines in Fig. 8 to the modern shoreline (i.e., the X intercepts of each regression) suggests that backfilling alluvium would have reached

the positions of the future modern shoreline, i.e., the canyon mouths, at ~19.5 ka in Tecelote Canyon, at ~12.1 ka in Verde Canyon, and at ~11.3 ka in Wreck Canyon.

5. Discussion

5.1. Reconstructing paleoshorelines and paleochannels

Because sea level is the local base level for the island's river systems, fluctuations of sea level exert a strong control on the timing and processes of erosion and aggradation. During the late Pleistocene and Holocene, eustatic sea level varied from as much as 8 m above present during the last interglacial (LIG) period about 120 ka (Muhs et al., 2011), to between −120 and −135 m below present sea level at the last glacial maximum (LGM) about 20 ka (Yokoyama et al., 2000; Clark and Mix, 2002; Peltier and Fairbanks, 2006). However, sea level at a specific location is also influenced by local or regional isostatic, tectonic, and gravitational movements of the Earth's crust. For example, relative sea level is affected by deflections of the ocean floor caused by isostatic movement of the solid earth in response to ice-ocean mass

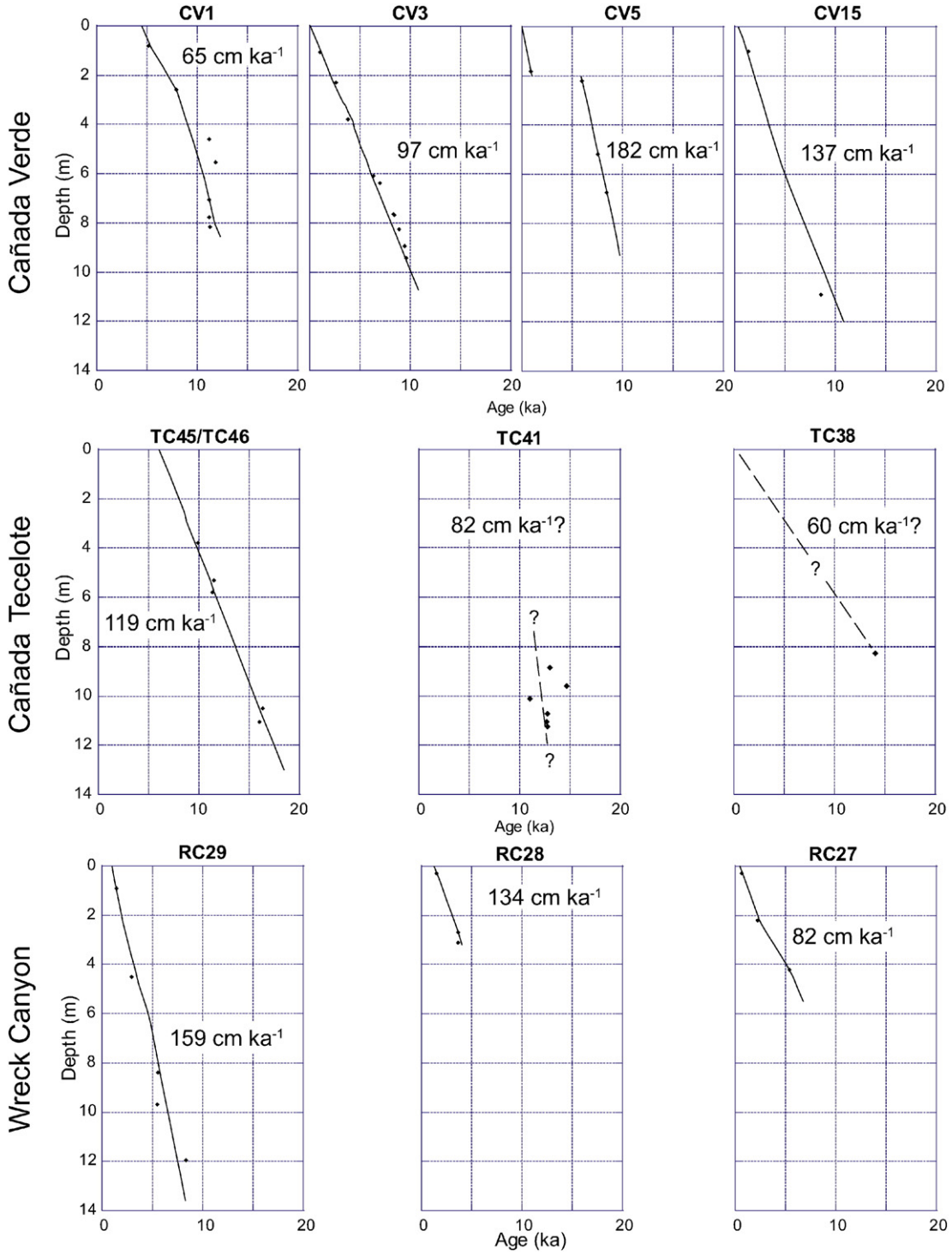

Fig. 7. Age-depth plots for alluvial sections in Cañada Verde, Cañada Tecelote, and Wreck Canyon. Solid lines were determined using the Bacon computer program (Blaauw and Christen, 2011). Dashed lines are hand-drawn estimates.

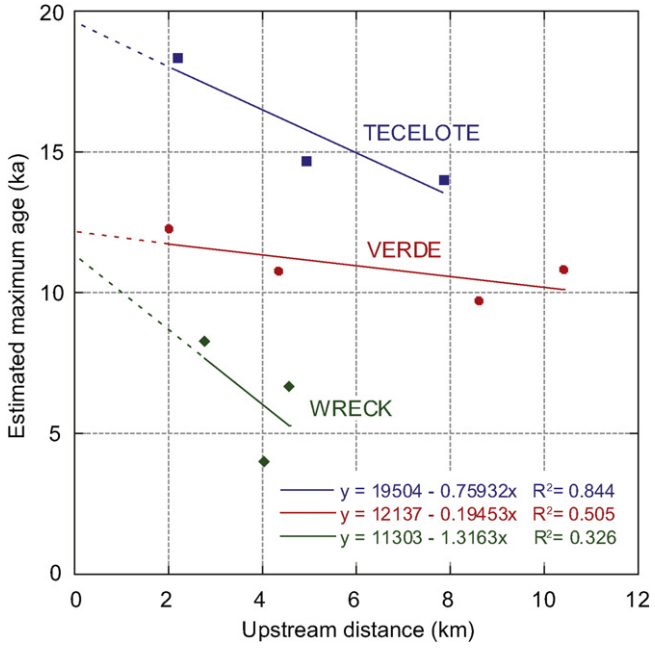

Fig. 8. Plots of estimated maximum age of alluvial stack versus distance upstream from modern shoreline for three drainages on SRI.

transfer during Quaternary glacial-interglacial cycles. The ocean surface elevation is also changed by gravitational attraction between glacial ice and ocean water, ocean water with itself, and between ocean water and land masses, which themselves are being deformed by ice or ocean loading or unloading (Farrell and Clark, 1976; Mitrovica and Milne, 2003; Milne and Mitrovica, 2008). Expansion and contraction of glacial ice sheets also affects the earth's rotation, which in turn, affects tides worldwide (Milne and Mitrovica, 1996). These local or regional departures from eustacy have been termed glacial isostatic adjustment (GIA) effects.

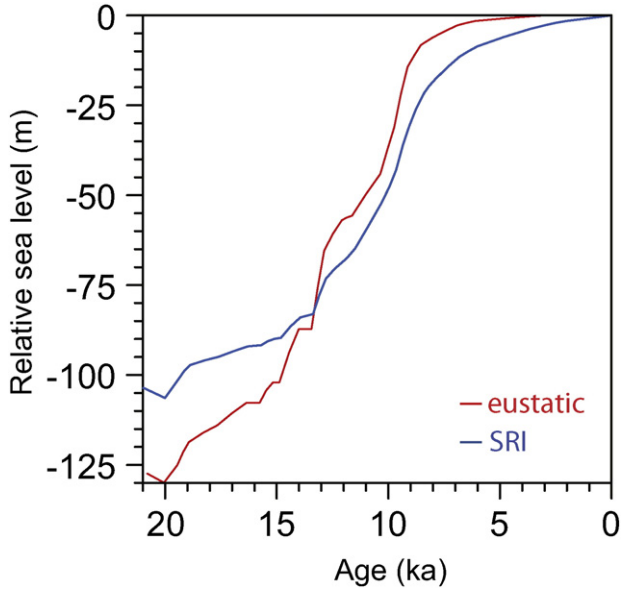

Fig. 9. Modeled relative sea-level curve for Santa Rosa Island (34°N, 120°W) incorporating GIA effects (in blue). For comparison, red curve is modeled global eustatic sea-level curve, based on glacial ice volume and mass-transfer models developed at Australian National University (ANU; Fleming and Lambeck, 2004). Redrawn from Clark et al. (2014).

A relative sea level (RSL) curve that incorporates adjustments for GIA effects has been modeled for the Channel Islands of California, and specifically for Santa Rosa Island (Fig. 9; Clark et al., 2014). The GIA-adjusted sea level curve differs significantly from the eustatic sea level curve at several points. For example, whereas the eustatic curve indicates that sea level at LGM was ~ — 130 m below present, the LGM sea level at SRI reached a minimum of ~ — 106 m. After 13 ka, the modeled RSL at SRI is as much as ~15 m lower than the eustatic curve, and RSL approaches modern sea level 2–3 ka later than the eustatic curve (Fig. 9).

The GIA-adjusted RSL curve was used with a DEM of bathymetry data to determine the locations of paleoshorelines around SRI at various times as sea level rose from its local LGM minimum to its present level (Fig. 10). The accuracy of the paleoshoreline reconstruction is highly dependent on the accuracy of the sea-level curve used. Because of the gentle slope of the shelf surrounding SRI, elevation differences of 15–30 m between the eustatic sea-level curve and a localized, GIA-adjusted curve could result in errors of hundreds to thousands of meters in the inferred paleoshoreline positions.

When sea level was lower than present, large areas of the shelf surrounding SRI were exposed, extending the channel lengths and drainage basin areas of streams on the island. ArcHydro Tools were used within ArcGIS to generate drainage lines on SRI and on the shelf surrounding the island by routing flow from DEM grid cells of higher elevation into lower elevation grid cells. Predictably, the modeled flow lines follow the existing drainages on the island. On the shelf, however, the flowpaths are very straight. The paleochannels on the shelf would probably be more sinuous than indicated by the modeled flowpaths, because as sea level rose following the LGM, the streams would likely have initially reduced their gradients by increasing sinuosity via lateral channel migration, which would also have increased valley width. Fluvial valleys on continental shelves are typically as much as 1–2 orders of magnitude wider than they are deep (Zaitlin et al., 1994). Modeling studies as well as direct observations suggest that deep valleys are generally not incised into a shelf unless sea level drops below the outer edge of the shelf (Koss et al., 1994; Woolfe et al., 1998; Ethridge et al., 2005), which did not occur at LGM around the northern Channel Islands. Possible topographic remnants of these valleys that are 1–2 km wide and 5–20 m deep can be seen in a cross section of the shelf surface north of Santa Rosa Island (Fig. 11). The drainage lines modeled by ArcGIS follow these shallow topographic lows.

Longitudinal profiles of three streams modeled using the GIS tools (Fig. 12) exhibit typical concave-up profiles for reaches above present sea level (0 m), but the now-submerged portions of the profiles follow the gradient of the marine shelf. This probably reflects partial to nearly complete filling of the stream channels with alluvial, eolian, and/or marine sediment. Such sediment-filled paleochannels might be located by seismic surveys or offshore coring, but in the absence of such data, we cannot determine if the modeled flowpaths on the shelf correspond to the actual locations and paths of the paleochannels. The flowpaths are, however, acceptable for the purposes of this study. Because the paleochannels would likely have been more sinuous than the modeled flowpaths, the flowpaths suggest a best-case scenario, i.e., the steepest possible channel gradients and shortest channel lengths of the offshore portions of the streams. Longer, less steep channels would further enhance the magnitude of aggradation and backfilling, but otherwise, the behavior of the system would be the same or extremely similar, so the modeled flowpaths are sufficient to illustrate the physical conditions on the shelf that dictated the fluvial systems' responses to sea-level changes.

5.2. Late Pleistocene aggradation on the shelf

The marine platform surrounding Santa Rosa Island has a considerably shallower gradient than those of the streams that drain onto the shelf (Fig. 12). This difference reflects the dominance of marine, rather

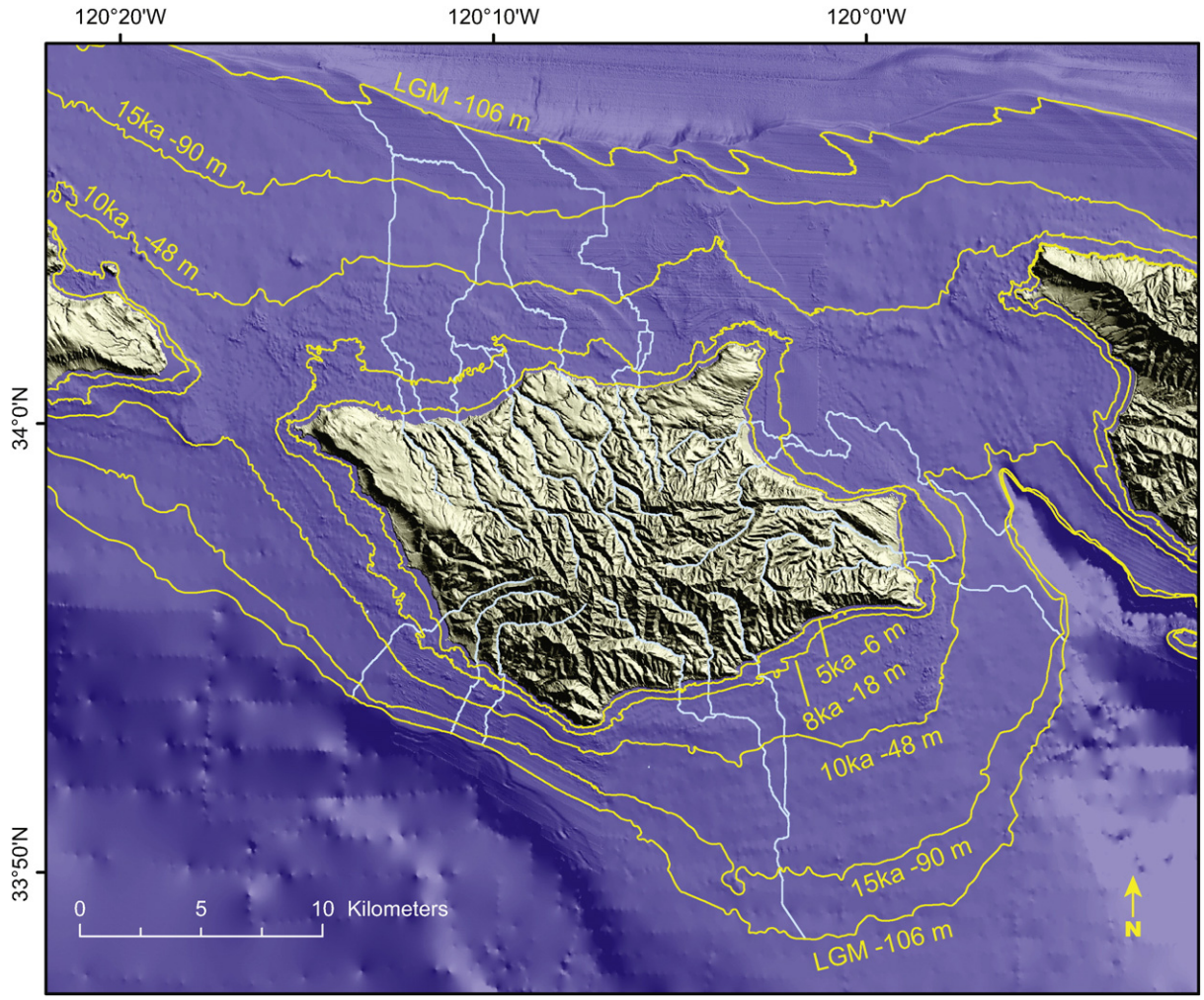

Fig. 10. Bathymetric/topographic map of Santa Rosa Island and the surrounding marine shelf. Elevation data from NOAA (Carignan et al., 2009). Paleoshorelines shown in yellow; dates and elevations from Fig. 9 (Clark et al., 2014). Light blue lines denote major drainages (onshore) and modeled locations of paleodrainages (shelf).

than terrestrial, landscape-forming processes. The gentle seaward slope and relatively flat topography of marine shelves resulted from the long-term erosional and depositional forces of waves, tidal fluctuations, storms, and nearshore ocean currents (e.g., longshore drift). These processes can either erode the marine platform surface or redistribute sediment across the platform in response to localized excesses or deficiencies of sediment relative to the energy of the ocean system. Other processes, such as tectonics and fluvial erosion/deposition, can modify the submerged marine platform surface, but subaerial processes become more important when the shelf is exposed during sea-level lowstands.

The proximal, or nearshore, portion of the marine platform also appears to have more topographic relief than the distal, or seaward, part (Figs. 10 and 11). Lobate features on the platform may be wedges of deltaic sediment deposited during the period of rapidly rising sea level (Fig. 10; Posamentier and Vail, 1988; Wright and Marriott, 1993). However, some of the topographic features on the platform may be remnants of eolian dunefields. Modeling by J.X. Mitrovica in Muhs et al. (2012) indicates that sea level was −55 to −75 m during marine oxygen isotope stage (MIS) 3 (~60–30 ka), after which sea level dropped to its LGM minimum, then rose again, reaching the break in slope between the nearshore platform and distal shelf at about 9–10 ka (Figs. 9, 10 and 12). Thus the proximal shelf was exposed from ~60 ka until ~10 ka. Eolian sand on SRI and the other Channel Islands is derived largely from eroded fragments of calcium-carbonate-rich, marine-invertebrate skeletal material from the sea floor. Prevailing winds from the northwest deflated these sands from the exposed shelves and blew them onto what are presently the land areas (Muhs et al., 2009). However, remnants of dunefields may have survived deflation and subsequent marine incursion on the platform and may form some of the topography offshore of Sandy Point and Carrington Point (Fig. 11). These dunes may have also filled and obscured some of the fluvial channels on the proximal shelf.

An alternative, and perhaps more likely, interpretation of the features on the shelf is that they are lobes of delta sediments. Fluvial aggradation on the shelf would be expected to occur in a considerably different manner than aggradation within the island's valleys because the channels are relatively unconfined on the shelf, whereas they are constrained within their valleys on land. As sea level rose and the shoreline progressed landward (Figs. 10 and 12), the streams would most likely have built relatively extensive deltas, spreading sediment laterally across the shelf rather than backfilling a single channel (Posamentier and Vail, 1988; Wright and Marriott, 1993; Zaitlin et al., 1994). The extent of delta building by each drainage would influence the rate at

which aggrading sediment reached each canyon mouth, in that building more or larger delta lobes would slow the upstream progression of an accretionary wedge. An additional consideration is the extent to which channels may have merged on the shelf, as well as the locations of such merging (Fig. 10). If sediment from multiple drainages were funneled into a single channel, channel infilling and/or delta deposition would presumably occur at a faster rate than from a drainage that retained a single channel for a long distance on the shelf, thereby influencing the rate of upstream sediment wedge migration. Conversely, a network of relatively evenly-spaced single channels would likely be more effective in distributing alluvium broadly across the shelf surface. If the drainages are roughly of equal size and length and the shelf gradient is relatively consistent in a shore-parallel direction, one might expect to see a roughly even landward progression of aggradation across the shelf, reaching the canyon mouths at approximately the same time. This is not indicated by the data in this study.

The gradient of the shelf profile (Fig. 12) exerts significant controls on river system behavior. For the same vertical change, the shoreline moves horizontally much farther along a gently sloping shelf surface than across a steeply sloping shelf. Off the north (Verde and Tecelote Canyons) and south (Wreck Canyon) coasts of SRI, the proximal (inner) shelf, immediately adjacent to the modern shoreline, has a much gentler slope than the onshore channel gradient. The gradient of the distal (outer) shelf steepens sharply below a break in slope at about −30 to −35 m water depth (Fig. 12). This gently sloping inner shelf surface is simply the modern marine platform, composed of a short (a few hundred meters) steep section closest to shore, then a more gently sloping section that can extend up to several kilometers offshore (Bradley and Griggs, 1976). The distal portion of the shelf is probably a submerged marine terrace bench.

Although the position of the advancing shoreline is a primary control, a number of other factors also influence the timing and rate of aggradation. Following the LGM, the climate, which exerts a major control on water and sediment supply, gradually became warmer and drier (Anderson et al., 2010). Discharge therefore probably decreased, but erosion of valley side slopes may have increased owing to loss of vegetative cover. Intrinsic processes and complex response of the system, causing out-of-phase erosion and deposition in different reaches, would have caused sediment to move downstream in irregular pulses (Schumm, 1993; Wright and Marriott, 1993).

The rate of sea-level change also varied during this period (Fig. 9). If base-level change is gradual, the channel is more likely to adjust its gradient by changing its sinuosity, whereas if base-level change is rapid, incision or aggradation is more likely (Schumm, 1993). Local channel size and shape, as well as shelf slope, would define the accommodation space (Posamentier and Vail, 1988) for sediment arriving at each point from upstream and thus influence the rate at which the alluvial wedge progressed upstream.

5.3. Aggradation in the canyons of Santa Rosa Island

The period between LIG and LGM, ~80-20 ka, was characterized primarily by erosion in upstream areas (i.e., landward of present sea level) and deposition on the distal regions of the shelf. This 60 ky span of falling sea level appears to have been sufficient time to have flushed most of the late Pleistocene alluvium from the valleys, in most places exposing the bedrock valley floor. This is indicated by the lack of alluvium samples dated older than ~16 ka in this study (Table 2), as well as in most previous studies that have dated alluvium from SRI (e.g., Orr, 1968; Colson, 1996; Kennett et al., 2008). One exception to this is

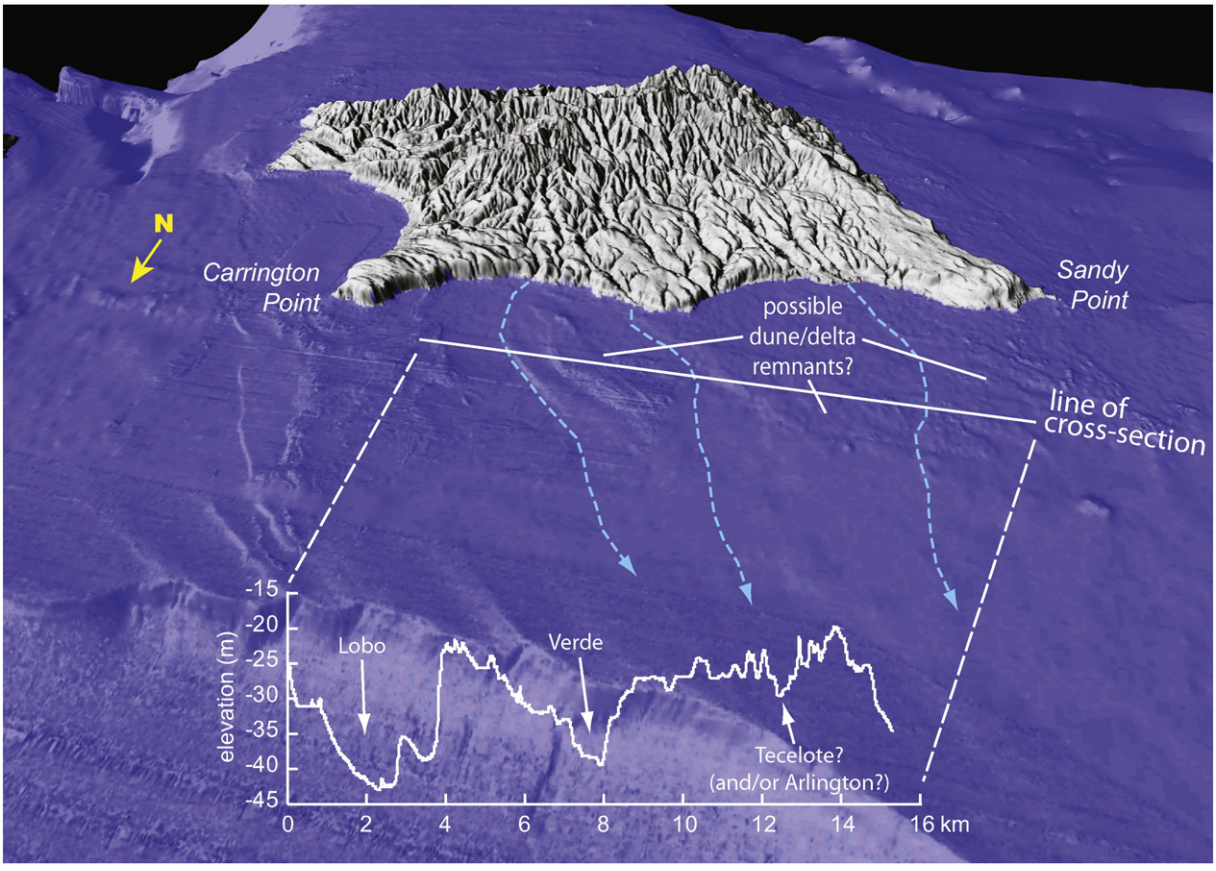

Fig. 11. Oblique three-dimensional aerial view looking south across marine shelf and SRI, and topographic cross section across portion of shelf. Image generated from NOAA topographic/bathymetric data (Carignan et al., 2009). White line denotes location of topographic section across marine platform surface. Vertical exaggeration of section is approximately 180:1.

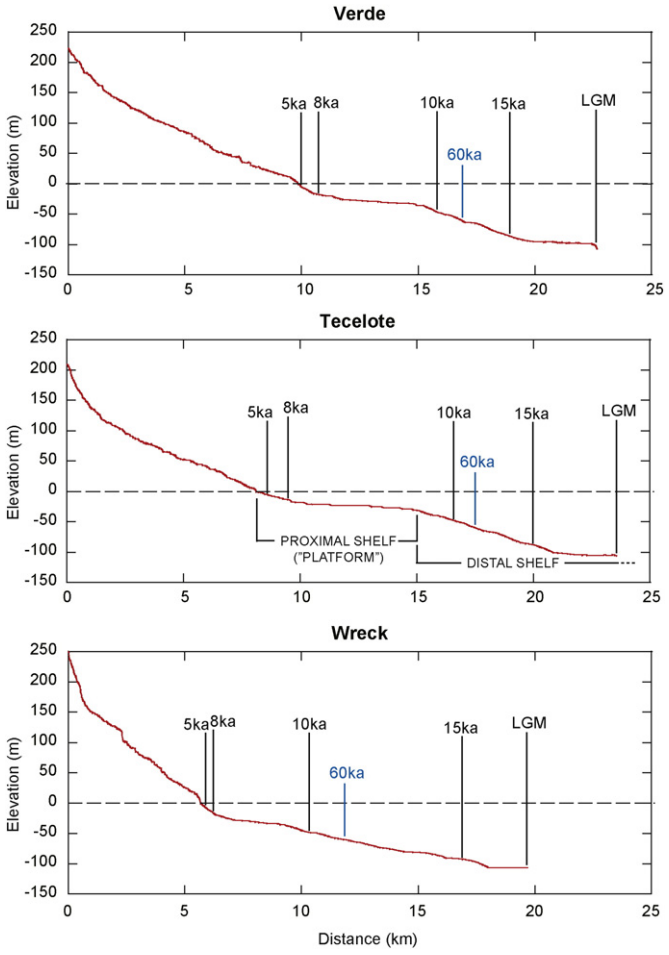

Fig. 12. Channel longitudinal profiles of three major drainages on SRI, extended to the postulated LGM (~21 ka) shoreline (data from Figs. 9 and 10). Postulated shoreline positions at 60, 21, 15, 10, 8, and 5 ka are indicated above profiles. Proximal shelf was exposed above sea level from ~60 to 10 ka.

charcoal collected near the base of the alluvial sequence in Cañada Verde at our station 52. At that locality, Pinter et al. (2011) reported calibrated ^{14}C ages of 25 and 29 ka at depths of 1105 cm and 1130 cm, respectively, whereas we obtained ages of 11.2 and 13.1 ka from charcoal collected at depths of 1005 and 1180 cm (Table 2). When the samples from this study are plotted with those from Pinter et al. (2011) on an age-depth plot (as in Fig. 7), our results form an essentially straight line, suggesting relatively continuous and steady deposition throughout the sedimentary profile. Using data from this study, the plot also closely resembles the age-depth plot for station 3 (Fig. 7), located 130 m upstream from station 52. In contrast, Pinter et al.'s older ages would require the presence of an unconformity corresponding to a depositional hiatus, which is not supported by our observations and data.

As sea-level began to rise following the LGM lowstand, backfilling of the island's canyons appears to have begun almost immediately, at least in Cañada Tecelote, which may have begun backfilling as early as ~19.5 ka (Fig. 8). Considering that Tecelote and Verde Canyons have similar relief, gradients, and channel lengths, the nearly 8000-year difference between the times when the aggradational wedge is estimated to have reached the modern positions of each canyon mouth appears to be anomalous. However, the interaction of the downstream-flowing river systems with the upstream-approaching shoreline is complex. Possible reasons for the different timings of alluvial wedge progression were discussed in the previous section.

The extensive areas of the shelf that were exposed during lowstands (Fig. 10) increased overall channel lengths to 2–4 times their highstand lengths (Fig. 12). The expanded drainage systems provided ample routing and, ultimately, storage on the shelf for older alluvial sediments as upstream reaches eroded and transported alluvium downstream. As sea level rose, stream lengths shortened. The rate of channel shortening on the shelf is controlled largely by the shelf gradient and the rate of sea level rise. North of SRI, the distal shelf is considerably steeper than the proximal shelf, whereas to the south, although divided by a similar break in slope, the outer shelf is only slightly steeper than the inner shelf (Fig 12). Between 20 and ~13 ka, sea-level change was relatively gradual, then sea level rose rapidly until ~8 ka (Fig. 9). Between ~20 and 10 ka, the channels of Verde and Tecelote Canyons shortened by ~7 km, but Wreck Canyon shortened by almost 10 km as a result of the more gentle slope of the outer shelf on the south side of the island (Fig. 12). After 10 ka, rapidly rising sea level across the gently sloping inner shelf shortened the channels of Verde, Tecelote, and Wreck canyons by 5, 8, and ~4.5 km, respectively, in only ~2000 years (Figs. 10 and 12). These values are useful for comparison because all three drainages had begun aggrading in their canyons by 11 ka (Fig. 8). After that time, because migration of the aggrading sediment wedge was confined between the valley walls, more aggressive channel shortening would likely drive more rapid advancement of backfilling sediment and,

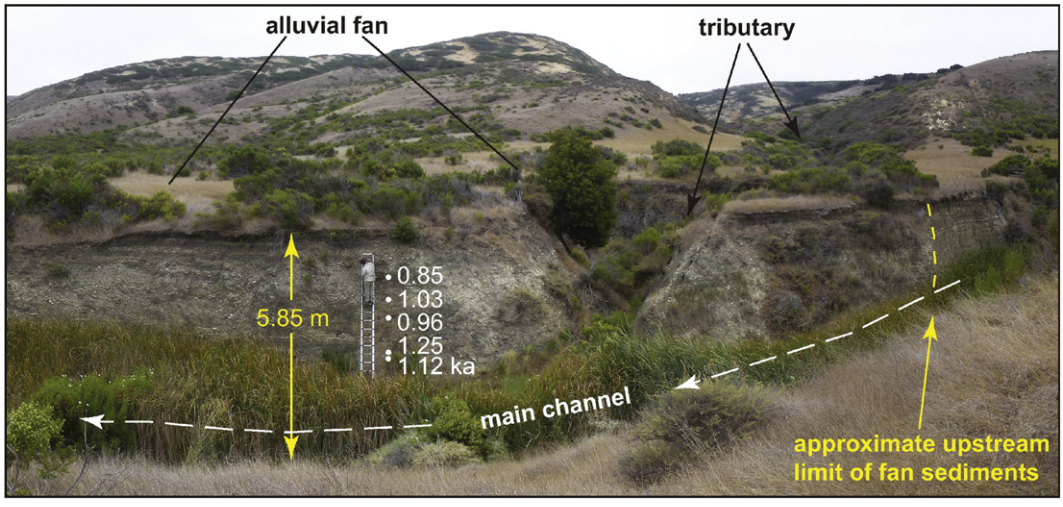

Fig. 13. Photo of station 11 (see Fig. 4 for location) in Cañada Quemada, looking southwest, showing stratigraphic positions and calibrated radiocarbon dates of charcoals and humic acid from alluvial fan sediments (Table 2). Fan originated from the tributary in background.

indeed, that appears to have been the case. Cañada Verde, which shortened the most after 10 ka, backfilled more rapidly than the other two streams (Fig. 8). This may also be in part because of the lower gradient of Cañada Verde relative to the other two drainages, assuming that other factors such as water and sediment discharge varied similarly in all drainages.

By 12–11 ka, most, if not all, of the island's valleys were aggrading, even though the paleoshoreline was still several kilometers from the canyon mouths (Figs. 10 and 12). The channels would have maintained and probably increased their sinuosities in response to the rising base level (Schumm, 1993). However, channel pattern adjustment was insufficient to compensate for the rapid rate and large magnitude of base-level change. At the leading edge of the upstream-advancing aggradational wedge, channel gradient was locally reduced, resulting in sediment deposition through frequent overbank flooding (Wright and Marriott, 1993), further reducing local channel and floodplain gradient and increasing flood frequency. This can be inferred from the multiple episodic depositional sequences in the alluvial fills of each drainage. Each sequence consists of sandy and clayey silts of overbank floods, capped by poorly to well-developed, organic-rich paleosols of floodplains. These probably remained wet for extended periods (Fig. 5), as indicated by presence of the valves of the nonmarine ostracodes *Candona*, *Cypridopsis*, and *Ilyocypris* in the sediments. Eventually, a minimum gradient threshold was reached, after which a shallow channel would be incised into the alluvium, indicated by pebble and gravel layers, but rapid accretion kept the channels relatively shallow (see, for example, the channel fill at station CV5 in Fig. 5). As the channels filled with sediment, overbank flooding would occur more frequently and the sequence would repeat.

The number, thickness, and frequency of these overbank flooding sequences vary between drainages, and between reaches of each drainage, although some depositional surfaces can be traced laterally for tens to hundreds of meters. Floodplain accretion was controlled by a number of factors. Because some proportion of sediment probably continued to be routed onto the exposed shelf, rates of delta building, channel filling, and avulsions, i.e., filling of the accommodation space (Posamentier and Vail, 1988) on the shelf, probably exerted a downstream control on the frequency and timing of overbank flooding in the inland valleys. This downstream control likely interacted in a complex manner with upstream controls, including water and sediment availability from source areas, resulting in complex responses causing phases of erosion, deposition, or rejuvenation in various reaches, despite the overall aggradational mode of the system.

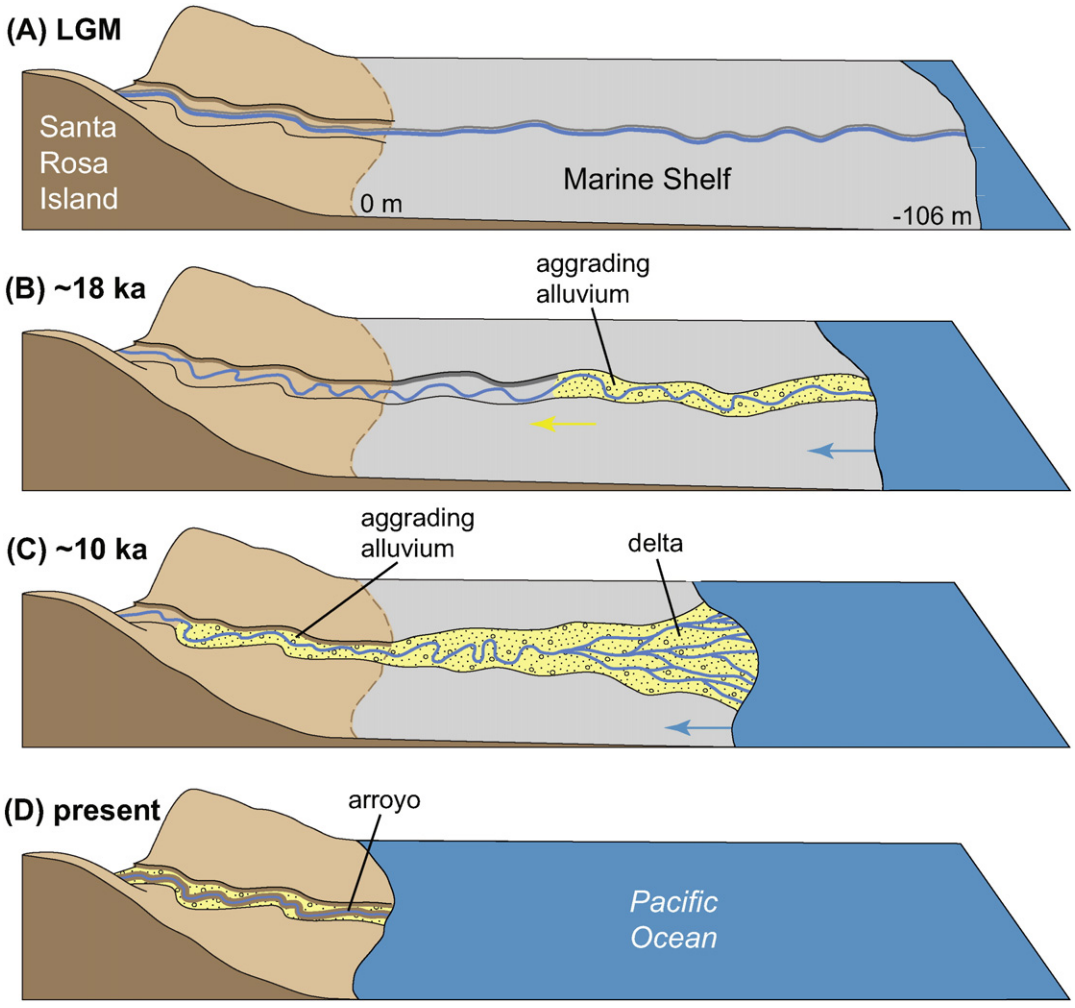

Fig. 14. Generalized time series illustrating postulated fluvial system response to post-glacial rising sea level. (A) At LGM (ca. 25–21 ka) the larger upland valleys were mostly free of accumulated sediment, and channels on the shelf were relatively straight, broad, and shallow. (B) As sea level rose, channels on the shelf reduced gradient by meandering, and alluvium began backfilling the channels. (C) By early Holocene, channels on the shelf were wide and filled with sediment, and deltas distributed sediment broadly across the shelf. Aggradational sediment wedges reached into most upland valleys. (D) Aggradation in upland valleys ceased at ~0.5–0.1 ka, then deep arroyos incised through as much as 14 m of valley alluvium.

An illustrative example of a complex response in the form of tributary rejuvenation was observed at station 11 in Quemada Canyon (Fig. 4). At this location, a large tributary enters the main channel and nearly 6 m of coarse-grained alluvial fan sediment, dating to ~1 ka, displaced the main channel to the opposite side of the canyon (Fig. 13, Table 2). The alluvial fan deposits persist for a few hundred meters downstream of the tributary junction, ultimately grading into the older and finer-grained floodplain sediments. We investigated tributary junctions in other drainages on SRI and did not find evidence of widespread tributary rejuvenation at 1 ka, therefore concluding that rejuvenation of this tributary was likely triggered by internal forcings rather than being part of an islandwide or regional event.

Dateable material was sought as close as possible to the top of each alluvial section to estimate the timing of cessation of aggradation. Surface soil samples were not collected to avoid the risk of modern disturbance and contamination. The youngest samples, ranging in age from ~0.5 to 1.5 ka, were collected at depths averaging ~1 m (Table 2), indicating that floodplain aggradation generally continued until at least 0.5 ka, probably even later. Extrapolating the fitted age-depth curves to the floodplain surface (i.e., depth of 0 cm) may provide estimates of the cessation of aggradation at each section (Fig. 7). For example, at station CV3, the age-depth line passes through the origin, suggesting that floodplain aggradation continued until the present, whereas at station RC29, the line meets the surface at ~0.8–0.9 ka (Fig. 7). For any floodplain surface with an extrapolated pre-modern age (i.e., the *X* intercept of the age-depth curve is >0), two possible interpretations are (i) the *X* intercept is a reasonable estimate of when floodplain accretion ceased at that location, or (ii) the floodplain is an erosional surface from which an indeterminate amount of sediment has been removed, so the *X* intercept represents a maximum estimate of the cessation of floodplain aggradation (i.e., aggradation ceased at that time *or later*). Excluding station CV1, which likely experienced some surface erosion because of its close proximity to a tributary drainage, estimates from all the sections with dated samples collected within ~1 m of the surface suggest that floodplain aggradation continued until at least 500 years ago (Fig. 7).

5.4. Shift from aggradational to erosional sedimentary regime

The long period of late Pleistocene-Holocene aggradation ended with the modern episode of major incision. Arroyos have incised the alluvium filling all of the canyons on SRI, cutting through as much as 12–14 m of accumulated floodplain sediment. It is this deep incision that provides access to the alluvial record. In most areas, the modern stream flows over bedrock or a very thin (typically <0.5 m) veneer of sediment, having abandoned the former Holocene floodplain which now forms terraces on one or both sides of the valleys (Fig. 2A, 2B). Arroyos have bisected Chumash archeological sites at several locations on the island (Kennett, 2005; Rick, 2007). For example, shell middens, dwellings, and burial sites dated to as late as 1820 CE in the Chumash village of Niaqla (Rick, 2007), on the northwest coast of the island, are cut by the arroyo of Skull Gulch, indicating that incision took place sometime after this date. Another shell midden, at a site designated CA-SRI-77, located at the eastern end of Bechers Bay, has been dated to as recently as ~1000 YBP (Rick et al., 2005) and is bisected by a deep arroyo. An early photograph of Santa Rosa Island, taken by Philip Mills Jones in 1901 during an archaeological survey (Jones, 1956, reproduced in Orr, 1968, and Woolley, 1998), shows a well-formed arroyo in Cañada La Jolla Vieja, suggesting that arroyo cutting took place prior to the beginning of the twentieth century, at least at this location.

Sedimentation rates have been estimated from cores collected from an estuarine marsh in Old Ranch Canyon (Cole and Liu, 1994; Anderson et al., 2010). For the 5000 years prior to 1800 CE, the sedimentation rate in the marsh was ~0.7 mm y^{-1}. During the early 1800s, the sedimentation rate in the marsh increased to an average of 13.4 mm y^{-1} and peaked at 23.0 mm y^{-1} between 1874 CE and 1920 CE (Cole and Liu, 1994), indicating that runoff increased significantly. Ranching began on Santa Rosa Island in 1844, and in the 1860s and early 1870s, as many as 100,000 sheep grazed on the island (Allen, 1996). Several periods of intense drought also occurred in the 1860s and 1870s. Extensive overgrazing and livestock loss due to starvation were documented on San Miguel, San Nicolas, and Santa Cruz Islands following the severe drought of 1863–1864 and subsequent droughts (Johnson, 1980). Catastrophic flooding caused by the storm of 1861–1862 that dropped as much as 1650 mm of rain on southern California in a 45-day period is reported to have initiated arroyo cutting in a number of locations (Engstrom, 1996), and it would have caused severe erosion of the denuded land surfaces on the island. Major floods also occurred in 1867 and 1891 (Engstrom, 1996). This combination of reduced vegetative cover caused by drought and/or overgrazing by sheep and episodes of severe flooding probably initiated arroyo cutting.

On neighboring Santa Cruz Island (SCI), valleys cut into bedrock contain incised alluvial fills (Brumbaugh, 1980; Perroy et al., 2012) similar to those observed on SRI. In contrast, however, the alluvium on SCI typically occurs in two distinct facies: a lower, fine-grained alluvium containing multiple organic-rich beds similar to the alluvial sequences on SRI, overlain by a coarser alluvial, colluvial, and debris-flow unit lacking substantial organic matter, which is not found on SRI. Charcoal and organics near the top of the fine-grained facies were dated to 1550 ± 80 ^{14}C YBP and 1555 ± 80 ^{14}C YBP (Brumbaugh, 1980), and it follows that the coarser-grained facies was deposited after this time. Some authors have suggested that this upper unit is the result of vegetation stripping by grazing animals in the late 1800s (Brumbaugh, 1980; Perroy et al., 2012). Drought and overgrazing in the late 1800s and early 1900s were also postulated to be the primary causes of severe erosion and sediment mobilization on San Miguel Island (Johnson, 1980).

By analyzing sedimentary data and historic topographic maps, Perroy et al. (2012) determined that arroyo formation in Pozo Canyon, on Santa Cruz Island, took place between 1875 and 1886, following a period of intense sheep overgrazing, severe drought in 1877, and a large rainstorm in 1878. They further used the thickness of post-grazing sediment and late Holocene sedimentation rates to suggest that a natural threshold for arroyo incision might have been reached within 100–300 years, had conditions favorable for incision not been accelerated by the untimely combination of intense livestock stress and unusual weather events (Perroy et al., 2012).

By 5 ka BP, sea level was only 6 m below present, and the rate of sea-level rise in the last 5000 years was extremely slow and gradual, in contrast to the rapid rise during the preceding 8000 years (Figs. 9, 10). As sea level stabilized, the aggradation rate would be expected to decrease, though likely with a time lag as the effects of the changes were transmitted upstream. No longer under the driving influence of continuing base-level rise, the stream systems would have soon reached a natural intrinsic threshold at which aggradation would slow or cease, followed by incision of arroyos as the systems adjusted to the relative stability of modern sea level (Schumm, 1973). Thus, arroyo formation would have eventually begun as an intrinsic system response, even in the absence of the vegetation stripping, drought stresses, and massive floods of the mid- to late nineteenth century.

6. Summary

The island setting of Santa Rosa Island provides an unparalleled environment in which to record and preserve the response of fluvial systems to major changes of sea level. The period of falling sea level between the end of the last interglacial highstand at ~80 ka and the last glacial lowstand at ~25–21 ka was marked by erosion and incision in the uplands and deposition of alluvial sediment on the distal shelf. Sea-level lowering was relatively gradual, falling ~100 m in 60,000 years. During this period, most of the alluvium in the main drainages was transported out of the island's valleys and onto the shelf via

relatively straight, shallow channels (Fig. 14A). Streams throughout the island probably incised into bedrock during this time.

Sea level rose relatively rapidly following the LGM lowstand of −106 m, attaining its present elevation after ca. 20,000 years, triggering a shift from an erosional to a dominantly depositional sedimentary regime. The system began adjusting to rising sea level by increasing channel sinuosity, thereby widening the channels by lateral migration. Accumulation of sediment occurred first through vertical and lateral accretion in broad, shallow, channels on the shelf. Aggradation was probably initially confined to the channels (Fig. 14B). As sea level continued to rise, however, channel avulsion and delta deposition distributed sediment broadly across larger areas of the shelf (Fig. 14C). The rate of sea-level rise did not correlate directly with alluvial aggradation rates. The gradient of the shelf determined the extent of fluvial channel shortening relative to shoreline advance, but the volume of sediment delivered by each drainage, and the extent to which the sediment was distributed across the shelf surface, also controlled the rate at which aggradational wedges progressed upstream across the shelf.

During the late Pleistocene and Holocene, backfilling of canyons (landward of present sea level) appears to have progressed in a more orderly and predictable fashion largely because the streams were confined within their valleys (Fig. 14C). Vertical aggradation locally reduced stream gradients, causing frequent overbank flooding, lateral channel shifting (meandering across the width of the valley), and after some minimum gradient threshold was reached, shallow incision into the alluvium. Channel accretion occurred fairly rapidly, again leading to frequent overbank flooding and deposition of fining-upward sequences of floodplain sediment. Local channel gradient and morphology, short-term climate variations, and internal controls also affected the timing and magnitudes of these cut, fill, and flood episodes and are reflected in the number and thickness of aggradational sequences.

Floodplain aggradation within the valleys continued until at least ~500 YBP, followed by intensive arroyo cutting that left the relict floodplains as alluvial terraces standing as much as 12–14 m above the present streams (Fig. 14D). Sedimentary and historical evidence points to overgrazing, drought, and floods in the mid- to late nineteenth century as factors that facilitated arroyo incision.

Acknowledgements

References

Allen, K.B., 1996. Ranching on Santa Rosa Island. In: Allen, K.B. (Ed.), Island of the Cowboys - Santa Rosa Island. Occasional Paper no. 7. Santa Cruz Island Foundation, Santa Barbara, CA, pp. 9–15.

Anderson, R.L., Byrne, R., Dawson, T., 2008. Stable isotope evidence for a foggy climate on Santa Cruz Island, California at ~16,600 cal. yr. B.P. Palaeogeogr. Palaeoclimatol. Palaeoecol. 262, 176–181.

Anderson, R.S., Starratt, S., Jass, R.M.B., Pinter, N., 2010. Fire and vegetation history on Santa Rosa Island, Channel Islands, and long-term environmental change in southern California. J. Quat. Sci. 25, 782–797.

Avila, F.A., Weaver, D.W., 1969. Middle Tertiary stratigraphy of Santa Rosa Island. In: Weaver, D.W., Doerner, D.P., Nolf, B. (Eds.), Geology of the Northern Channel Islands. American Association of Petroleum Geologists and Society of Economic Paleontologists and Mineralogists, Pacific Sections, Special Publication, pp. 48–67.

Blaauw, M., Christen, J.A., 2011. Flexible paleoclimate age-depth models using an autoregressive gamma process. Bayesian Anal. 6, 457–474.

Blum, M.D., Tornqvist, T.E., 2000. Fluvial responses to climate and sea-level change: a review and look forward. Sedimentology 47 (Suppl. 1), 2–48.

Bradley, W.C., Griggs, G.B., 1976. Form, genesis, and deformation of Central California wave-cut platforms. Geol. Soc. Am. Bull. 87, 433–449.

Brumbaugh, R.W., 1980. Recent geomorphic and vegetal dynamics on Santa Cruz Island, California. In: Power, D.M. (Ed.), The California Islands: Proceedings of a Multidisciplinary Symposium. Santa Barbara Museum of Natural History, Santa Barbara, CA, pp. 139–158.

Carignan, K.S., Taylor, L.A., Eakins, B.W., Warnken, R.R., Lim, E., Medley, P.R., 2009. Digital Elevation Model of Santa Barbara, California: Procedures, Data Sources and Analysis. NOAA Technical Memorandum NESDIS NGDC-29. U.S. Dept. of Commerce, Boulder, CO.

Clark, J., Mitrovica, J.X., Alder, J., 2014. Coastal paleogeography of the California-Oregon-Washington and Bearing Sea continental shelves during the latest Pleistocene and Holocene: implications for the archaeological record. J. Archaeol. Sci. 52, 12–23.

Clark, P.U., Mix, A.C., 2002. Ice sheets and sea level of the Last Glacial Maximum. Quat. Sci. Rev. 21, 1–7.

Cole, K.L., Liu, G., 1994. Holocene paleoecology of an estuary on Santa Rosa Island, California. Quat. Res. 41, 326–335.

Colson, K.B., 1996. Neotectonics of the Left-lateral Santa Rosa Island Fault, Western Transverse Ranges, Southern California (Unpublished M.S. Thesis) San Diego State University.

Colson, K.B., Rockwell, T.K., Thorup, K.M., Kennedy, G.L., 1995. Neotectonics of the left-lateral Santa Rosa Island fault, western Transverse Ranges, southern California. Geological Society of America Abstracts With Programs, Cordilleran Section. 7, p. 11.

Crouch, J.K., 1979. Neogene tectonic evolution of the California continental borderland and western Transverse Ranges. Geol. Soc. Am. Bull. 90, 338–345.

Davis, W.M., 1902. Base-level, grade, and peneplain. J. Geol. 10, 77–111.

Dean, W.E., 1974. Determination of carbonate and organic matter in calcareous sediments and sedimentary rocks by loss on ignition: comparison with other methods. J. Sediment. Petrol. 44, 242–248.

Dibblee, T.W., Ehrenspeck Jr., H.E., 1998. General geology of Santa Rosa Island, California. In: Weigand, P.W. (Ed.), Contributions to the Geology of the Northern Channel Islands, Southern California. American Association of Petroleum Geologists, Pacific Section, Miscellaneous Publication MP-45, pp. 49–75.

Engstrom, W.N., 1996. The California storm of January 1862. Quat. Res. 46, 141–148.

Ethridge, F.G., Germanoski, D., Schumm, S.A., Wood, L.J., 2005. The morphological and stratigraphical effects of base-level change: a review of experimental studies. In: Blum, M.D., Mariott, S.B., Leclair, S.F. (Eds.), Fluvial Sedimentology VII. International Association of Sedimentologists Special Publication 35, pp. 213–241.

Farrell, W.E., Clark, J.A., 1976. On postglacial sea level. Geophys. J. R. Astron. Soc. 46, 647–667.

Fleming, K., Lambeck, K., 2004. Constraints on the Greenland ice sheet since the last glacial maximum from sea-level observations and glacial-rebound models. Quat. Sci. Rev. 23, 1053–1077.

Johnson, D.L., 1980. Episodic vegetation stripping, soil erosion, and landscape modification in prehistoric and recent historic time, San Miguel Island, California. In: Power, D.M. (Ed.), The California Islands: Proceedings of a Multidisciplinary Symposium. Santa Barbara Museum of Natural History, Santa Barbara, CA, pp. 103–121.

Jones, P.M., 1956. Archaeological investigations on Santa Rosa Island in 1901. In: Heizer, R.F., Elsasser, A.B. (Eds.), University of California Anthropological Records. 17(2), pp. 201–280.

Junak, S., Knapp, D.A., Haller, J.R., Philbrick, R., Schoenherr, A.A., Keeler-Wolf, T., 2007. The California Channel Islands. In: Barbour, M.G., Keeler-Wolf, T., Schoenherr, A.A. (Eds.), Terrestrial Vegetation of California, (3rd Ed) University of California Press, Berkeley, CA, pp. 229–252.

Kennett, D.J., 2005. The Island Chumash: Behavioral Ecology of a Maritime Society. University of California Press, Berkeley, CA.

Kennett, D.J., Kennett, J.P., West, G.J., Erlandson, J.M., Johnson, J.R., Hendy, I.L., West, A., Culleton, B.J., Jones, T.L., Stafford Jr., T.L., 2008. Wildfire and abrupt ecosystem disruption on California's Northern Channel Islands at the Ållerød-Younger Dryas boundary (13.0–12.9 ka). Quat. Sci. Rev. 27, 2530–2545.

Koss, J.E., Ethridge, F.G., Schumm, S.A., 1994. An experimental study of the effects of base-level change on fluvial, coastal plain and shelf systems. J. Sediment. Res. B64, 90–98.

Mackin, J.H., 1948. Concept of the graded river. Geol. Soc. Am. Bull. 59, 463–512.

Milne, G.A., Mitrovica, J.X., 1996. Postglacial sea-level change on a rotating earth: first results from a gravitationally self-consistent sea-level equation. Geophys. J. Int. 126, F1–F8.

Milne, G.A., Mitrovica, J.X., 2008. Searching for eustacy in deglacial sea-level histories. Quat. Sci. Rev. 27, 2292–2302.

Minor, S.A., Bedford, D., Schmidt, K.M., Schumann, R.R., Muhs, D.R., 2012. The ups and downs of the Santa Rosa Island fault, northern Channel Islands. California: More Than Simple Strike SlipAbstract T33A-2647, 2012 Fall Meeting. American Geophysical Union, San Francisco, CA.

Mitrovica, J.X., Milne, G.A., 2003. On post-glacial sea level: I. General theory. Geophys. J. Int. 154, 253–267.
Muhs, D.R., Skipp, G., Schumann, R.R., Johnson, D.L., McGeehin, J.P., Beann, J., Freeman, J., Pearce, T.A., Rowland, Z.M., 2009. The Origin and Paleoclimatic Significance of Carbonate Sand Dunes Deposited on the California Channel Islands during the Last Glacial Period. In: Damiani, C.C., Garcelon, D.K. (Eds.), Proceedings of the 7th California Islands Symposium. Institute for Wildlife Studies, Arcata, CA, pp. 3–14.
Muhs, D.R., Simmons, K.R., Schumann, R.R., Halley, R.B., 2011. Sea-level history of the past two interglacial periods: new evidence from U-series dating of reef corals from south Florida. Quat. Sci. Rev. 30, 570–590.
Muhs, D.R., Simmons, K.R., Schumann, R.R., Groves, L.T., Mitrovica, J.X., Laurel, D., 2012. Sea-level history during the last interglacial complex on San Nicolas Island, California: implications for glacial isostatic adjustment processes, paleozoogeography and tectonics. Quat. Sci. Rev. 37, 1–25.
Muhs, D.R., Simmons, K.R., Schumann, R.R., Groves, L.T., DeVogel, S.B., Minor, S.A., Laurel, D., 2014. Coastal tectonics on the eastern margin of the Pacific Rim: late quaternary sea-level history and uplift rates, Channel Islands National Park, California, USA. Quat. Sci. Rev. 105, 209–238.
Murray-Wallace, C.V., Woodroffe, C.D., 2014. Quaternary Sea-Level Changes: A Global Perspective. Cambridge University Press, New York.
Orr, P.C., 1968. Prehistory of Santa Rosa Island. Santa Barbara Museum of Natural History. Santa Barbara, CA.
Peltier, W.R., Fairbanks, R.G., 2006. Global glacial ice volume and last glacial maximum duration from an extended Barbados sea level record. Quat. Sci. Rev. 25, 3322–3337.
Perroy, R.L., Bookhagen, B., Chadwick, O.A., Howarth, J.T., 2012. Holocene and Anthropocene landscape change: arroyo formation on Santa Cruz Island, California. Ann. Assoc. Am. Geogr. 102, 1229–1250.
Pinter, N., Scott, A.C., Daulton, T.L., Podoll, A., Koeberl, C., Anderson, R.S., Ishman, S.E., 2011. The Younger Dryas impact hypothesis: a requiem. Earth-Sci. Rev. 106, 247–264.
Posamentier, H.W., Vail, P.R., 1988. Eustatic controls on clastic deposition II – sequence and systems tract models. In: Wilgus, C.K., Hastings, B.S., Kendall, C.G.S.C., Posamentier, H.W., Ross, C.A., Van Wagoner, J.C. (Eds.), Sea-Level Changes: An Integrated Approach. Society of Economic Paleontologists and Mineralogists Special Publication. 42, pp. 125–154.
Powell, J.W., 1875. Exploration of the Colorado River of the West and its Tributaries. U.S. Government Printing Office, Washington, D.C.
Reimer, P.J., Bard, E., Bayliss, A., Beck, J.W., Blackwell, P.G., Bronk Ramsey, C., Grootes, P.M., Guilderson, T.P., Haflidason, H., Hajdas, I., Hatte, C., Heaton, T.J., Hoffmann, D.L., Hogg, A.G., Hughen, K.A., Kaiser, K.F., Kromer, B., Manning, S.W., Niu, M., Reimer, R.W., Richards, D.A., Scott, E.M., Southon, J.R., Staff, R.A., Turney, C.S.M., van der Plicht, J., 2013. IntCal13 and Marine13 radiocarbon age calibration curves 0–50,000 years cal BP. Radiocarbon 55, 1869–1887.
Rick, T.C., 2007. Household and community archaeology at the Chumash village of Niaqla, Santa Rosa Island, California. J. Field Archeol. 32, 243–263.
Rick, T.C., Kennett, D.J., Erlandson, J.M., 2005. Preliminary report on the archaeology and paleoecology of the Abalone Rocks Estuary, Santa Rosa Island, California. In: Garcelon, D.K., Schwemm, C.A. (Eds.), Proceedings of the Sixth California Islands Symposium, Ventura, California, December 1–3, 2003National Park Service Technical Publication CHIS-05-01. Institute for Wildlife Studies, Arcata, CA, pp. 55–63.
Schumann, R.R., Minor, S.A., Muhs, D.R., Pigati, J.S., 2014. Landscapes of Santa Rosa Island, Channel Islands National Park, California. Monographs of the Western North American Naturalist. 7, pp. 48–67.
Schumm, S.A., 1973. Geomorphic thresholds and complex response of drainage systems. In: Morisawa, M. (Ed.), Fluvial Geomorphology. State University of New York, Binghamton, pp. 299–310.
Schumm, S.A., 1993. River response to baselevel change: implications for sequence stratigraphy. J. Geol. 101, 279–294.
Schumm, S.A., Brakenridge, G.R., 1987. River responses. In: Ruddiman, W.F., Wright Jr., H.E. (Eds.), North America and adjacent oceans during the last deglaciationThe Geology of North America, v. K-3. Geological Society of America, Boulder, CO, pp. 221–240.
Slingerland, R.L., Snow, R.S., 1988. Stability analysis of a rejuvenated fluvial system. Z. Geomorphol. 67, 93–102 N.F. Suppl-Bd.
Stuiver, M., Reimer, P.J., 1993. Extended ^{14}C database and revised CALIB radiocarbon calibration program. Radiocarbon 35, 215–230.
Vedder, J.G., Howell, D.G., 1980. Topographic evolution of the southern California Borderland during late Cenozoic time. In: Power, D.M. (Ed.), The California Islands: Proceedings of a Multidisciplinary Symposium. Santa Barbara Museum of Natural History, Santa Barbara, CA, pp. 7–31.
Weaver, D.W., Doerner, D.P., 1969. Lower Tertiary stratigraphy, San Miguel and Santa Rosa Islands. In: Weaver, D.W., Doerner, D.P., Nolf, B. (Eds.), Geology of the Northern Channel Islands. American Association of Petroleum Geologists and Society of Economic Paleontologists and Mineralogists, Pacific Sections, Special Publication, pp. 30–46.
Western Regional Climate Center, 2015. Summary of Weather Data From the Remote Automated Weather Station (RAWS) on Santa Rosa Island, California, for the Period 1991–2014. http://www.wrcc.dri.edu (accessed 10 Sep 2015).
Woolfe, K.J., Larcombe, P., Naish, T., Purdon, R.G., 1998. Lowstand rivers need not incise the shelf: an example from the Great Barrier Reef, Australia, with implications for sequence stratigraphic models. Geology 26, 75–78.
Woolley, J.J., 1998. Aspects of the Quaternary geology of Santa Rosa Island, California. In: Weigand, P.W. (Ed.), Contributions to the geology of the Northern Channel Islands, Southern California. American Association of Petroleum Geologists, Pacific Section, Miscellaneous Publication. MP-45, pp. 103–110.
Wright, V.P., Marriott, S.B., 1993. The sequence stratigraphy of fluvial depositional systems: the role of floodplain sediment storage. Sediment. Geol. 86, 203–210.
Yokoyama, Y., Lambeck, K., de Dekhar, P., Johnston, P., Fifield, L.K., 2000. Timing of last glacial maximum from observed sealevel minima. Nature 406, 713–716.
Zaitlin, B.A., Dalrymple, R.W., Boyd, R., 1994. The stratigraphic organization of incised-valley systems associated with relative sea-level change. In: Dalrymple, R.W., Boyd, R., Zaitlin, B.A. (Eds.), Incised-valley Systems. SEPM Special Publication. 51, Tulsa, Oklahoma, pp. 45–60.